ABSTRACT

DAVID WILLIAM ROBERTS. The Aerodynamic Analysis and Aeroelastic Tailoring of a Forward-Swept Wing. (Under the direction of Dr. Charles E. Hall, Jr.)

The use of forward-swept wings has aerodynamic benefits at high angles of attack and in supersonic regimes. These consist of reduction in wave drag, profile drag, and increased high angle of attack handling qualities. These increased benefits are often offset due to an increase in structural components, to overcome flutter and wing tip divergence due to high loading of the wing tips at high angles of attack. The use of composite materials and aeroelastic tailoring of the structures eliminates these instabilities without a significant increase in weight. This work presents the design of an aeroelastic wing structure for a highly forward-swept wing, and the verification of the aerodynamic and structural finite element analysis through experimental testing.

THE AERODYNAMIC ANALYSIS AND AEROELASTIC TAILORING OF A FORWARD-SWEPT WING

By

DAVID WILLIAM ROBERTS

A thesis submitted to the Graduate Faculty of
North Carolina State University
In partial fulfillment of the
Requirements for the Degree of
Master of Science

AEROSPACE ENGINEERING

Raleigh, NC
2006

APPROVED BY:

_____	_____
Dr. Charles Hall, Jr.	**Dr. Kara Peters**
Advisory Committee Chairman	**Advisory Committee Member**

_____
Dr. James Selgrade
Advisory Committee Member

DEDICATION

This research as well as my entire college career has been dedicated to my mother Susan R. Cox. Without her continuous love and support I would not be the person I am today.

BIOGRAPHY

David William Roberts was born on September 2, 1981 in Shreveport, Louisiana to Jay and Susan Roberts. He grew up in West Palm Beach, Florida along with his older siblings John and Christina. He moved to Roanoke Rapids, North Carolina in 1994 and graduated from Roanoke Rapids High School in May of 2000. He graduated from North Carolina State University in May of 2004 with a Bachelor of Science degree in Aerospace Engineering. He pursued his Master of Science degree in August of 2004 with the Flight Research program at North Carolina State University. David plans on obtaining this degree in addition to a minor in Mathematics in May of 2006. He has accepted a career in the Flight Test and Evaluation Division of NAVAIR in Patuxent River, Maryland.

ACKNOWLEDGEMENTS

I would like to first thank my advisor Dr. Charles E. Hall, Jr. and Mr. Stearns B. Heinzen for their guidance throughout my undergraduate and graduate career at North Carolina State University. I also express gratitude to my committee members Dr. Kara J. Peters and Dr. James F. Selgrade.

Furthermore, this project would not have been possible without the additional support of my fellow colleagues Mr. Drew P. Turner and Mr. Joseph M. Morrow. I would like to also thank my family and friends for their patience and support during my time at North Carolina State University. I extend a special appreciation to Ms. Sara M. Boseman for her endearing support throughout my college career.

TABLE OF CONTENTS

LIST OF TABLES

LIST OF FIGURES

LIST OF SYMBOLS

A	Airfoil Specific Constant
B	Airfoil Specific Slope
Bi-CF	0/90 Degree Orientation Carbon Fiber
b	Wing Span
C_l	Local Lift Coefficient
C_L	Total Lift Coefficient
$C_{L\ max}$	Maximum Lift Coefficient
C_{Lo}	Lift Coefficient at Zero Angle of Attack
$C_{L\alpha}$	Lift Curve Slope
C_m	Local Moment Coefficient
C_p	Pressure Coefficient
$C_{p\ lower}$	Lower Surface Pressure Coefficient
$C_{p\ upper}$	Upper Surface Pressure Coefficient
c_r	Root Chord
c_t	Tip Chord
D_{ij}	Matrix relating out of plane moments to out of plane deformations
E	Modulus of Elasticity
E_1	Modulus of Elasticity in the 1st Principle or Longitudinal Axis
E_2	Modulus of Elasticity in the 2nd Principle or Transverse Axis
FG	Fiberglass
G	Shear Modulus
q	Dynamic Pressure
S	Wing Area
Uni-CF	Uni-directional Carbon Fiber
α	Angle of Attack
ΔC_p	Pressure Coefficient Difference
Λ_{LE}	Leading Edge Sweep
$\Lambda_{c/4}$	Quarter Chord Sweep
Γ_w	Wing Dihedral
$\mu\varepsilon$	Microstrain
ν	Poisson's Ratio
ρ	Density
σ	Stress
$\sigma_{1\ max}$	Maximum Stress in the 1st Principle or Longitudinal Axis
$\sigma_{2\ max}$	Maximum Stress in the 2nd Principle or Transverse Axis

1 INTRODUCTION

Aircraft designers take advantage of wing sweep to improve handling qualities and aerodynamic efficiencies of aircraft at high angles of attack and in supersonic flight regimes. Throughout history swept-wing aircraft are most commonly aft-swept; although it has been long recognized that forward-swept wings yield many of the same benefits with an added increase in aerodynamic efficiency[1]. The benefits of the forward over aft sweep consist of improved lateral control at high angles of attack, reduction in wing profile drag, increased fuselage design freedom permitting fuselage contouring to minimize wave drag, and reduced trim drag[2]. Forward-swept wings are often not a viable option because of the potential for aerodynamic and structural instabilities at high angles of attack. Forward-swept wings are subject to aerodynamic forces that tend to twist the wing about an axis that is along the angle of wing sweep and off perpendicular to the fuselage. This results in high loading at the wing tips, which creates an unstable load case. This wing loading may lead to flutter or wing tip divergence, and ultimately result in structural failure. To avoid this, coupling between out of plane moments and deformations must be induced to overcome the airframe failure. To increase the coupling of forces and moments in an isotropic or metal wing requires numerous stiffeners at an angle to the wing axis[3]. The added members result in weight and cost penalties, offsetting the aerodynamic benefits of the forward sweep. The use of orthotropic composite materials has made it feasible to consider forward sweep as a viable option if the layers of the composite laminate are at various angles to the wing axis. These lightweight materials are significantly stiffer in the direction of the fibers than the transverse direction. Therefore the material properties of the composite induce an out of plane moment when an in

plane deflection occurs. Furthermore, advances in materials and manufacturing have increased the strength and reduced the cost of composite materials, allowing them to become a common feature in many aircraft components.

Another important aspect of the design process is the ability to analytically predict the aerodynamic and structural performance of the aircraft. The use of computer aided design and analysis packages has greatly increased the capability of the aircraft designer and reliance on these programs has grown extensively over the years. One such example is the Boeing 777, which was the first jetliner to be almost completely digitally designed using three-dimensional modeling analysis technology[4]. While more than 3 million parts were represented in the analysis and virtual mock-up, an iron-bird was still essential for the integration of the electronics, hydraulics, and internal dynamics of the aircraft. Although the analysis packages have numerous benefits, each program has limitations and emphasis must be stressed on the assumptions the program makes. Complex designs and/or advanced materials may be affected by the assumptions and experimental testing is necessary to confirm theoretical predictions.

The purpose of this work is to design the aeroelastic structures of a highly forward-swept wing and validate the aerodynamics and structural analysis programs used in the design process. The wing structure was designed to be capable of withstanding a wing loading ratio of 50 to 1. Prior to the structural design, experimental testing was conducted to validate the aerodynamic computations of CMARC for a forward-swept wing. This was accomplished by testing a rigid wind tunnel model with 52 pressure ports. Material testing of composite candidates was then performed to obtain the material properties that were loaded into the structural analysis program ANSYS.

The design of the tailored wing consisted of uni-directional carbon fiber, fiberglass, and a honeycomb core material. Ultimately, validation of ANSYS was conducted through physical and wind tunnel testing.

2 RESEARCH PROJECT OVERVIEW

2.1 Background

Over the past century, a significant amount of data has been collected on forward-swept wings. The data collected ranges from simple flat plates used in wind tunnel testing for determining static divergence, to the modern X-29A aircraft used for extensive flight testing. Each test increases the understanding of the aerodynamics, structural divergence, and handling characteristics of the forward-swept wing. For instance, it was previously determined that when a highly forward-swept wing is in the moderate lift range (C_L ~ 0.5 to 0.7), a vortex persists over the wing and induces a strong inward flow. This results in turbulent separation that causes a chordwise redistribution and a rearward shift in the aerodynamic center, with no loss of lift[5]. Above the moderate lift range, the wing generates leading edge tip vortices, causing separation at the root of the wing. A decrease in lift occurs and changes in the spanwise loading create an extremely large forward shift in the aerodynamic center[5]. Though general trends of the aerodynamics and structural divergence can be concluded from prior research, the designer is unable to precisely predict the effects of flow separation through correlation of previous data. In addition, the structural design for each test consists of different component geometries, placement, and materials; thus complicating the correlation of the models' structural divergence.

For decades the potential-flow field effects have been well understood and accurate methods of predictions are available; this is not the case for effects caused by flow separation[6]. Potential flow panel codes are extensively used to accurately calculate the pressure distribution of an object prior to separation of the flow. The low order panel code

PMARC is one such code previously used at North Carolina State University and has shown excellent agreement between theoretical and experimental pressure distributions when tested on a 45 degree aft-swept wing at 4 degrees angle of attack[7]. Other advanced programs such as Fluent, OVERFLOW, and MEMS use a finite volume method to solve the full Naviar-Stokes equations. This enables an approximate prediction of the effects on the pressure distribution for laminar separation bubbles and other regions of limited flow[8]. Modeling objects in these programs is both time and financially consuming; requiring multiple programs to generate the mesh or grid, compute the results, and post-processing of the data. Another approach to incorporate the effects of flow separation into the aerodynamic model is to modify the predicted potential flow field with wind tunnel results. This approach was used in the design of the X-29A and was attempted in this research.

For the structural analysis of the complex X-29A technology demonstrator aircraft, the aerodynamic loads obtained from FLEXSTAB were modified to represent the wind-tunnel-derived aerodynamics[9]. The aerodynamic computations of FLEXSTAB are based on a finite element method used to solve the linearized potential flow equations[10]. Similar to CMARC used in this research, the potential flow method used to calculate the pressure distribution is invisid and requires modification to aerodynamic loads to accurately depict visid flow effects obtained through wind tunnel testing. Upon completion of the aerodynamic model, the X-29A was iteratively appraised by structural analysis, weight optimization, and divergence analysis programs to determine the geometry and fiber orientation of the structures[11]. Ultimately, the aircraft was flight tested to evaluate the structural limits, aerodynamics, and advanced control systems throughout the entire flight envelope.

2.2 Wing Description

The general wing planform was designed during the 2004-2005 Aerospace Engineering Senior Design course at North Carolina State University (NCSU). The Archangel UAV features a forward-swept wing with an aft swept canard. The constructed aircraft is shown in Figure 1.

Figure 1: Archangel UAV

The parameters of the full-scale wing are listed in Table 2-1

Table 2-1: Archangel Wing Parameters

Wing Parameter	Value
Airfoil	NACA 6315
c_r	19.2 in.
c_t	12.0 in.
S	936 in.^{2}
b	60 in.
Λ_{LE}	-27.4 deg.
$\Lambda_{c/4}$	-30.0 deg.
Γ_w	3.8 deg.

The selected planform was scaled to 1:2 for use in the NCSU wind tunnel. This scale was selected by examining two parameters, the wingspan with respect to the tunnel width and the maximum blockage of the wing.

Table 2-2: Wing Parameters

Wing Parameter	Value
c_r	9.6 in.
c_t	6.0 in.
S	234 $in.^2$
b	30 in.

Using the geometric dimensions in Table 2-2, the limiting parameters were examined. The restriction for the wingspan is that it is less than 80 % the wind tunnel width and the maximum blockage must not exceed 7.5 %[12]. The 1:2 scale produces a wingspan that is approximately 67 % the width of the wind tunnel and has a blockage of 5.6 % at 20 degrees angle of attack.

2.3 Wind Tunnel Description

The low speed recirculating wind tunnel used is located at North Carolina State University. Its dimensions are 32 in. high, 45 in. wide, and 46 in. in length with a maximum dynamic pressure of approximately 13.0 psf. The operational temperature range is from approximately 65 F to 100 F. The tunnel has a turbulence factor of 0.33%[13].

Figure 2: NC State Closed-Circuit Wind Tunnel

2.4 Data Collection

2.4.1 Pressure Measurement System

A Scanivalve system with a Validyne P305 pressure transducer was used to acquire static pressures. The Scanivalve Digital Interface Unit (SDIU) was used to convert the analog transducer signal to digital. The P305 transducer has a pressure accuracy of +- 0.25% with temperature error less than 2% /100 F. Vinyl tubing was used to connect the pressure system to static ports throughout the wing. A linear calibration of the transducer was preformed by varying pressures in a water monometer and recording the voltage. The pressures ranged from +/- 3.0 in. H_2O with 0.5 in. H_2O increments. This resulted in a calibration slope of 1.424 and intercept of 0.008. A Gauss interpolation was not used for the calibration because the mean square error was 0.0002.

2.4.2 Wing Tunnel Balance

To obtain the aerodynamic force and moment coefficients, a half-inch 6-component internal strain gage balance was used. The NCSU wind tunnel testing guidelines set the limits of the balance at 20 pounds vertical force and a 20 pound-inch moment. The installed balance is shown in Figure 3.

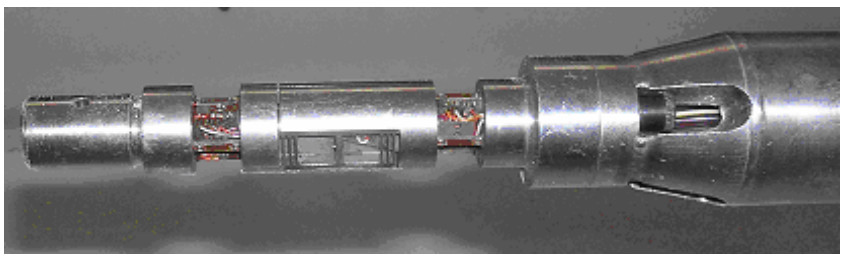

Figure 3: 6-Component Balance

With the selected wing size, the vertical and moment limit can be exceeded depending on the combination of alpha and dynamic pressure. The vertical load limit can be exceeded only at dynamic pressures and alphas approaching the maximum. However, the moment limits are exceeded well before any of these combinations due to the mounting location of the wing. Therefore, a large restriction was imposed when using the balance. Figure 4 shows the limits on alpha and dynamic pressure due to pitching moment.

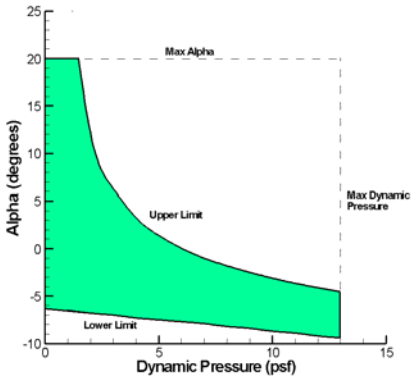

Figure 4: Wind Tunnel Limits

To avoid damaging the balance, the aerodynamic coefficients were calculated by obtaining data within the limits at dynamic pressures of 1.5, 3, 9, 11, and 13 psf. The "dummy balance" in Figure 5 was used to test the pressure port and tailored wing at dynamic pressures ranging from 9-11 psf. and angles of attack from 0 to 20 degrees. The pressure port wing was used for the aerodynamic analysis and contained 52 pressure ports while the tailored wing was used to verify the structural analysis of ANSYS and was outfitted with 9 strain gages.

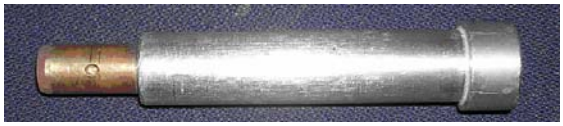

Figure 5: Dummy Balance

2.4.3 Strain Measurement System

A Vishay 6100 stress analysis data scanner was used to acquire strain values. The scanner is capable of recording data on each channel at rates up to 10,000 samples per second and holding up to 20 input cards with one channel per card. For the experimental testing performed in this research, only 5 cards were used at a scanning rate of 100 samples per second.

Figure 6: Vishay 6100 Scanner

The Vishay 6010 strain gage input card was used for analog-to-digital conversion. The card contains a fixed low-pass anti-aliasing filter with a programmable digital filter. The card has a measurement range of +/- 16,380 με and resolution of +/- 0.5 με. The calibration of the strain gage is accurate to +/- 3mV, which corresponds to +/- 0.2 με with the selected resolution and excitation voltage. The temperature stability is +/- 0.0005 % per F.

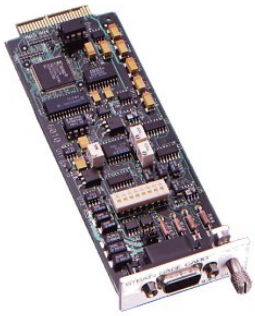

Figure 7: Vishay 6010 Input Card

The Vishay Micro-Measurements strain gage used for the experimental testing was an EA-06-060LZ-120. The grid dimensions are 0.075 in. by 0.075 in.. The strain limit is 3 % with a fatigue life of 10^6 cycles at +/-1500 με. The resistance at 75 F is 120.0 +/-0.3% with a gage factor of 2.075 +/-0.5 %. The temperature range for static strain measurements is – 100 F to 350 F. When the temperatures varies within the wind tunnel from 65 F to 100 F, the gage factor changes by less than 0.13 %. This change in the sensitivity of the strain gage directly relates to a change in the strain value by an equivalent percent. The change in strain was not accounted for in the data due to the fact that a 0.13 % change in the maximum strain obtained during the wind tunnel testing correlates directly to a 0.13 change in microstrain, which within the resolution of the measurement system, +/- 0.5 με.

3 MANUFACTURING

A hollow monolithic wing was used to increase the accuracy of the ANSYS analysis, simplify the routing of the pressure lines, and ease the manufacturing of the pressure ports. For the structural analysis, the thickness of the airfoil violates restrictions for thin-walled shells throughout regions other than the trailing edge; where as the 1/8th inch composite skin does not[14]. Therefore, without the use of a non-linear polystyrene or Styrofoam core, the ANSYS three-dimensional model can solely contain shell elements. This eliminates the combination of solid and shell elements with ideal bonds between the composite skin and foam core. More importantly, the use of tapered composites in the linear layered SHELL 99 element restricts the use of shell-to-solid submodeling[15].

For multiple wing skins to be consistent in geometry and easily manufactured, a plug and mold approach was used.

Figure 8: Plug and Mold

4 AERODYNAMICS

4.1 Introduction

The understanding and verification of the pressure distribution of the wing is vital for the structural design and analysis. To evaluate the pressure distribution of the forward-swept wing, theoretical calculations from the low-order panel code CMARC were used. CMARC is an invisid aerodynamic analysis program and testing of a wind tunnel model was used to accurately predict the viscous flow effects. Surface pressures of the model were obtained from 52 pressure ports at various span and chordwise location. Prior to flow separation, the spanwise lift distribution was calculated using a linear relationship between the change of pressure coefficients on the upper and lower surfaces and C_l. A tuft analysis was performed to visually observe the surface flow and verify conclusions on the viscous flow effects from the pressure port data.

4.2 CMARC

4.2.1 Background

The aerodynamic analysis software CMARC version 3.6 was used to generate the pressure distribution of the wing. CMARC is an invisid, low-order panel code derived from NASA's PMARC - Panel Method Ames Research Center. Since CMARC is an invisid panel method, it is not capable of modeling/calculating skin friction drag, or flow separation. CMARC is proficient in analyzing both laminar and turbulent boundary layers when the flow is attached. The analysis of the boundary layer is a two-dimensional procedure and the accuracy of the model diminishes near regions of separation, vortex formation, or if significant crossflow exists[16]. Therefore, for valid results, it is limited to the low and moderate lift regions, typically angles of attack less than +/- 6.0 degrees. These limits were exceeded to enable a comparison of the pressure distribution between the theoretical and experimental tests throughout the entire lift range. This allowed for estimates of locations and angles of attack in which CMARC was invalid to be obtained and the proper modification to the distribution to be determined.

4.2.2 Geometry and Pressure Distribution

To increase the accuracy of the CMARC model, a significant number of panels were used with special attention to regions where high pressure gradients occur. Furthermore, time-stepping the wake allowed for the deflection of the separation plane. Deflecting the wake increases the physical representation of the flow off of the trailing edge of the wing. Over 5000 panels were used for the CMARC analysis. Full cosine spacing of the panels was

used to decrease the panel size near the leading and trailing edges. The CMARC geometry described is shown in Figure 9.

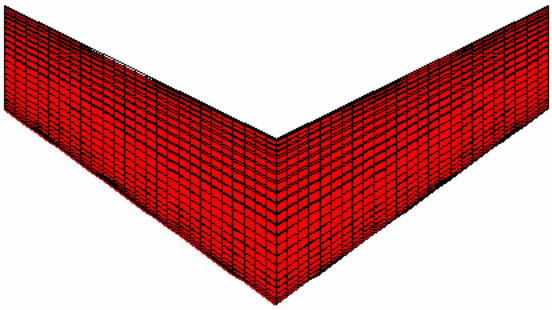

Figure 9: CMARC Panel Geometry

The pressure distributions on the upper surface at zero and 6 degrees angle of attack can be seen in Figure 10 and Figure 11.

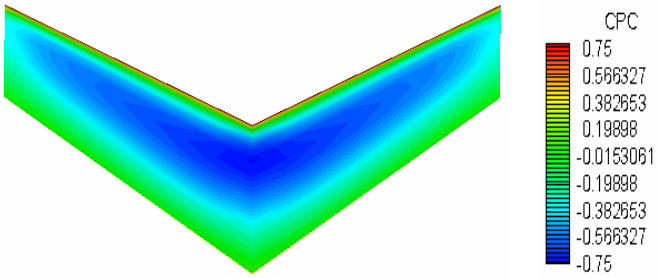

Figure 10: CMARC Pressure Distribution at an Alpha of 0.0 Degrees

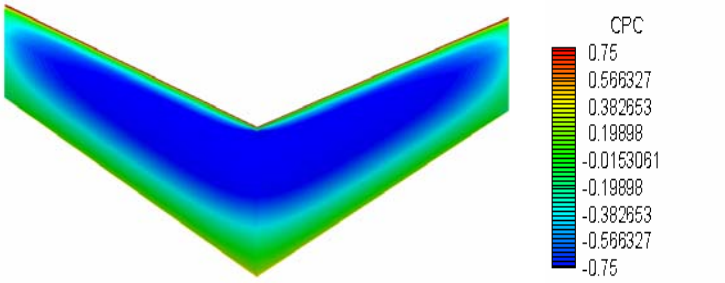

Figure 11: CMARC Pressure Distribution at an Alpha of 6.0 Degrees

As expected, the forward-swept wing has a higher C_l at the root of the wing prior to stall. In the high lift region, the root stalls while the lift at the wing tips continue to increase, thus resulting in high loading of the wing tips. To determine the pressure coefficient at each pressure orifice, the Fortran code in Appendix 8.1 was written. The executable uses the CMARC out file to calculate the approximate pressure at each port by interpolating the four nearest C_p values enclosing the port. Each C_p value used for the interpolation was within 5 percent chord and span of the port, with much lower percentages towards the leading and trailing edges.

4.3 Pressure Port Wing

To validate the pressures obtained from CMARC, a wind tunnel model with over 50 pressure ports was used. The wing was constructed with a wet lay-up and vacuum bag process. The wing was significantly overbuilt to ensure structural stability of the model. According to ANSYS, deflecting less than a 1/32 of an inch under the theoretical aerodynamic loads from CMARC.

4.3.1 Port Locations

The port locations were selected to provide efficient chord and spanwise pressure distributions. Regions with wing tip vortices or interference from the balance were avoided to increase the accuracy and consistency of the chord and spanwise distributions. Orifices located in these undesirable regions would result in inconsistent pressures when a vortex exists on the surface surrounding the pressure port and approximations for C_l using only two pressure ports would no longer be valid.

Two 16 port chordwise distributions were located on the left wing at 33.0 and 80.0 percent span. In addition, 20 ports were distributed spanwise on the upper and lower surfaces at 33 percent chord, a location which provides the most accurate and reliable pressures for estimated the local lift coefficient[17]. The chord and spanwise locations for each orifice is listed in Appendix 8.2.

4.3.2 Manufacturing of Ports

Typical pressure ports are manufactured with stainless steel tubulations that are mounted perpendicular to the surface. This method is convenient for airfoil sections with ample volume. One such example is the wing tested in the NCSU wind tunnel with a 12 in. chord and NFL-0414F airfoil.

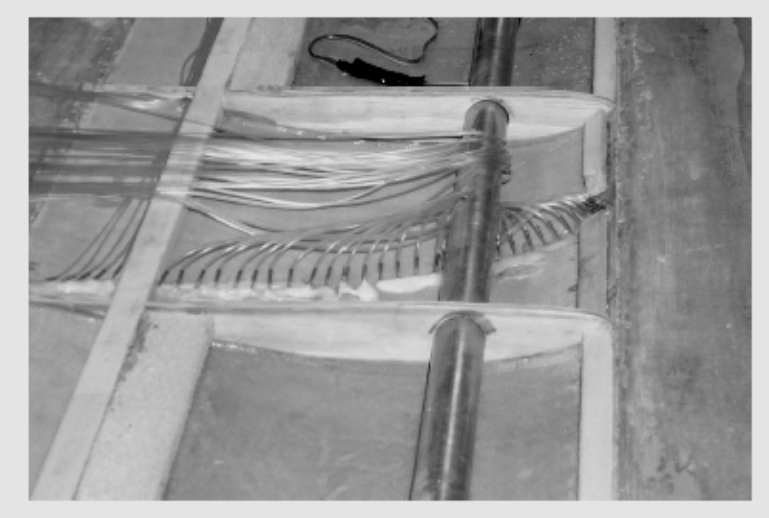

Figure 12: Pressure Ports[18]

To reduce cost and allow for orifices to be positioned near the trailing edge of the pressure port wing, stainless tubulation was not used in combination with the vinyl pressure tubing. Instead the 0.40 inch tube was attached parallel to the skin with a metal insert extending from the tube and through the orifice. The tube and insert were covered in a two-part epoxy mixed with a Kevlar fiber filler to increase the volume and thickness of the epoxy.

The description previously listed can be seen in Figure 13.

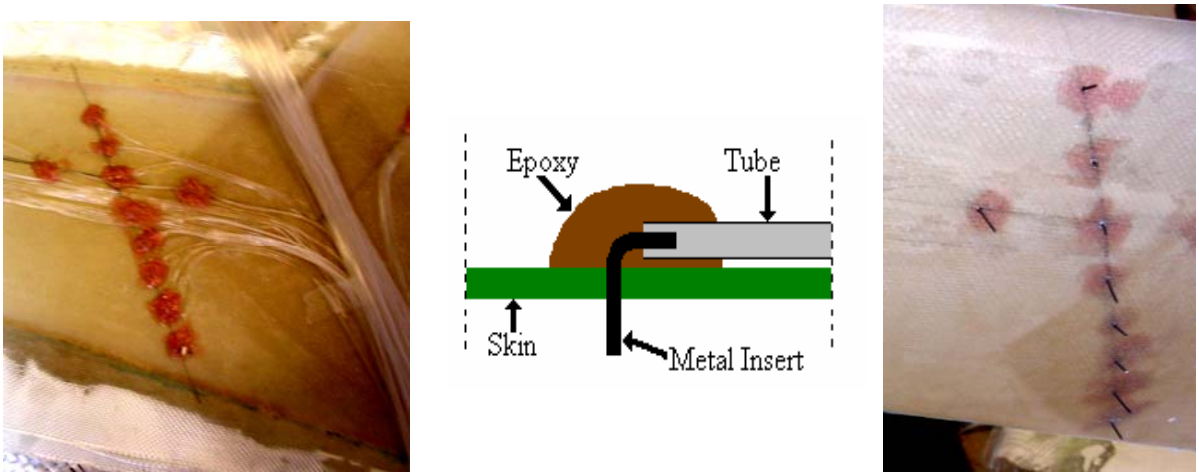

Figure 13: Pressure Port Manufacturing

Prior to wind tunnel testing, the metal inserts were removed and a pressure test was performed to ensure that there were no leaks in system. From this test it was found that ports 10, 14, and 44 would produce invalid pressures. Ports 10 and 14 are located on the upper surface at 80 % span and at 18.7 and 64.4 percent chord respectively. Port 44 is located on the upper surface at 68.3 % span, 33 % chord. Therefore, a cubic interpolation of the surrounding ports was used to estimate the pressure coefficient at the location of the ports that failed the pressure tests.

4.3.3 Manufacturing Error

Although the major geometric properties of the mold such as airfoil shape, sweep, dihedral, and span all have relatively low percentage errors, the manufactured skins have an abrupt angle on the lower surface near the trailing edge. The percent errors between the design and manufactured wing geometry are listed in Table 4-1.

Table 4-1: Manufacturing Errors

Geometric Property	Manufactured Geometry	Percent Error
c_r	9.72 in.	1.3
c_t	6.03 in.	0.5
Λ_{LE}	-26.8 deg.	2.2
Γ_w	4.0 deg.	5.3
b	29.97 in.	0.1

The error in the trailing edge occurred when the skins were bonded together. The skins also have a slightly higher trailing edge in this region, similar to reflex in the airfoil. This affects lift and pitching coefficients as well as the stall angle of attack. The region covers approximately 2.5 % of the chord and causes a 2.0 % reduction in C_l at a 0 angle of attack. The change in CMARC geometry is shown in Figure 14.

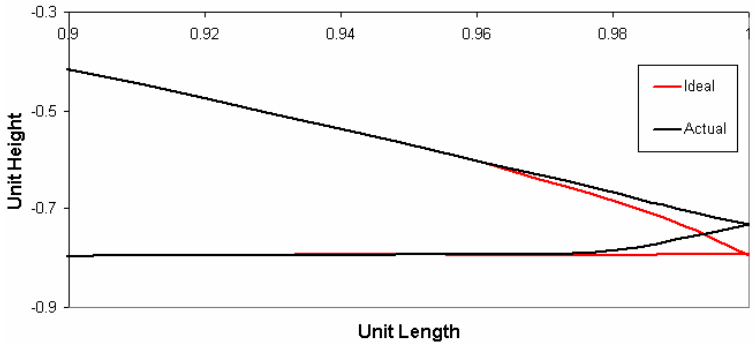

Figure 14: Modified CMARC Trailing Edge

The change in pressure distribution at 33 % span between an ideal trailing edge and the manufactured airfoil is shown in Figure 15.

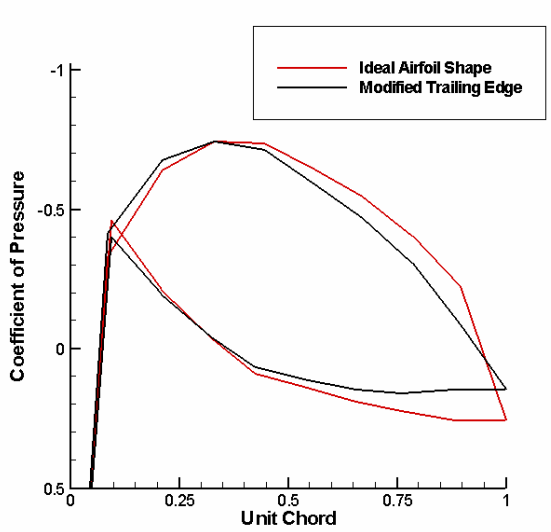

Figure 15: Trailing Edge Effects in CMARC at Alpha = 0 Degrees

Since the pressure coefficients obtained from the wind tunnel tests were compared to the CMARC pressure distributions, the geometry of the manufactured pressure port wing was used in the CMARC instead of the designed geometry. The CMARC pressure distribution using the manufactured wing geometry was also loaded into ANSYS for the structural analysis. The only geometric feature altered for the structural analysis was the dihedral angle, which had the highest percent error between the design and manufactured geometry.

4.4 Wind Tunnel Testing

To validate the pressure distribution calculated from CMARC, a rigid wind tunnel model was used. Each test was conducted at a dynamic pressure of 9.0 to prevent the wind tunnel from overheating during testing. The wing mounted to the wind tunnel sting is shown in Figure 16.

Figure 16: Pressure Port Test in NCSU Wind Tunnel

To evaluate the Reynolds number effects, a comparison between dynamic pressures of 9.0, 11.0, and 13.0 psf. was performed. The maximum difference between the pressure coefficients was 14.2 % on the lower surface trailing edge and 2.9 % on the upper surface at 56 % chord. It was concluded that the difference in pressures on the lower surface was due to the abrupt angle on the lower surface near the trailing edge. The sudden change in the slope of the surface causes the flow to separate near the trailing edge. The turbulent flow in this region becomes stronger with an increase in Reynolds number, resulting in a larger suction. The differences in the upper surface pressures are relatively low error, although

comparisons at 18.7 and 64.4 percent chord were estimated because ports 10 and 14 failed pressure tests previously conducted. The comparison at 0.0 degrees angle of attack is shown in Figure 17.

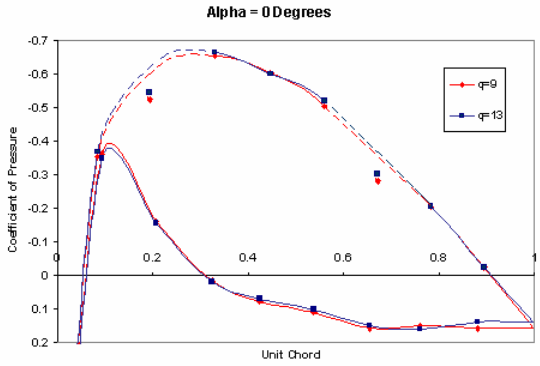

Figure 17: Dynamic Pressure Effects on the Airfoil Pressure Distribution

Remaining within the limits of the balance, the aerodynamic coefficients from wind tunnel testing were determined and compared to CMARC. The coefficients were calculated at a dynamic pressure of 9.0 and are listed in Table 4-2:

Table 4-2: Aerodynamic Coefficients

	Wind Tunnel	CMARC	% Error
C_{Lo}	0.359	0.337	6.1
$C_{L\alpha}$ (per deg.)	0.054	0.060	11.1
$C_{L\ max}$	1.15 @ ~ 14.5 deg.	---	---

It was concluded that the error between the analytical and experimental values was due to viscous effects. The viscid flow effects are also increased due to the surface roughness of the wing, which causes the transition from laminar to turbulent flow to occur earlier than predicted. Another contributing factor in the reduction of the $C_{L\alpha}$ was the separation of flow due to the abrupt angle on the lower surface near the trailing edge, which CMARC is not capable of modeling.

4.4.1 Chordwise Pressure Distribution

Pressure data was collected from each port at alphas ranging from 0 to 18 degrees and at a dynamic pressure of 9.0. Each pressure was compared with theoretical values obtain from CMARC. The pressure plots for multiple alpha cases are available in Appendix 8.3. Figure 18 and Figure 19 show a comparison between wind tunnel results and CMARC predictions. The left and right plot pressures are located at 80 and 33 percent span respectively. Since pressure ports 10 and 14, located in the plots on the left side failed the pressure tests, a cubic interpolation of the surrounding points was used.

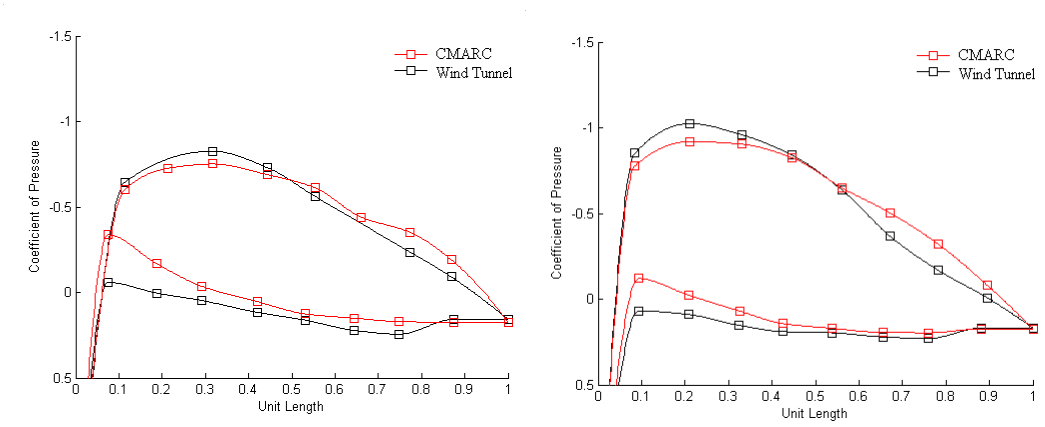

Figure 18: 2-D Pressure Distribution at Alpha = 6 Degrees

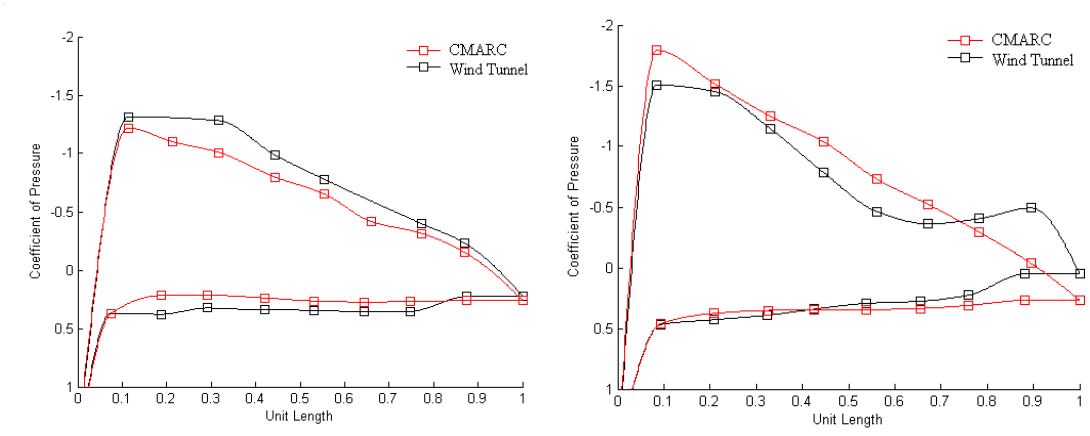

Figure 19: 2-D Pressure Distribution at Alpha = 16 Degrees

From these plots, it is clear that the root C_l is initially much higher than the tip. This higher C_l results in the flow to begin separating at 33 % span at an alpha of ~12 degrees while the flow at 80 % span remains attached at 18 degrees. The continual increase in the wing tip C_l results in a high loading of the wing tips. The transfer of loading from the root to the wing tip was shown by comparing the change in C_l with respect to the angle of attack for the 33 and 80 percent span locations.

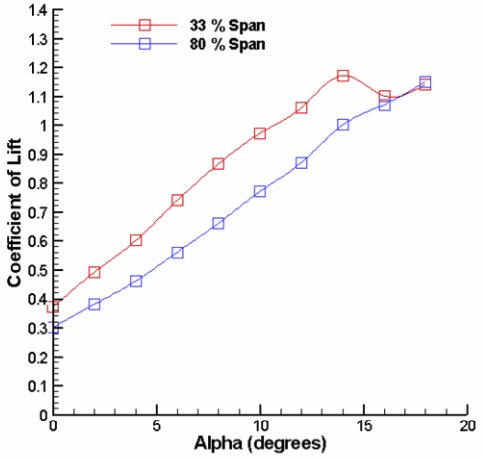

Figure 20: Comparison of Spanwise Lift Coefficients

The largest difference between the predicted and experimental pressures is an increase in the pressure coefficient on the upper surface between 50 and 90 percent chord. This is important to the structural design because the pitching moment was larger than expected, thus increasing the loading on the main spar and deflection of the leading edge. Prior to stalling the airfoil, this difference in pressure coefficients was almost 40 % near the root. The increase in the pressure coefficient is due to the inward crossflow induced by vortices during the moderate lift region. The crossflow was visually observed during the tuft analysis in Chapter 4.4.3. Once flow separation occurs, the suction on the upper surface is approximately 20 times stronger than predicted in regions near the trailing edge.

4.4.2 Spanwise Lift Distribution

The local lift coefficient is typically obtained by integrating the coefficients of pressure at a select chordwise location. To obtain the pressures, multiple chordwise pressure orifices are used. However, the manufacturing time, supplies, and data acquisition systems can become very costly. A viable option to reduce these expenses is to use pairs of pressure ports located in the vertical plane on the upper and lower surface between 30.0 and 40.0 percent chord[17]. This dramatically reduces the number of pressures ports necessary to obtain the spanwise lift distribution. Obtaining the pressure difference between the select ports will allow for approximation of the local lift by use of equation 1.

$$C_l = A + B\Delta C_p \qquad 1^{17}$$

Where ΔC_p is defined according to equation 2.

$$\Delta C_p = C_{p_{lower}} - C_{p_{upper}} \qquad 2^{17}$$

The chordwise wind tunnel pressures obtained at 33.0% span were used to solve for the airfoil specific constants *A* and *B*. Approximations of C_l were performed by using the program in Appendix 8.4, which utilizes cubic or spline interpolations and simple integration of the pressure coefficients to calculate the C_l. Overall, the cubic interpolation method provides a more accurate representation of the pressure distribution than the linear or spline methods, which have unrealistic changes in the slopes of pressures. The maximum difference in C_l values between the three methods was 4 % at an alpha of 18 degrees.

The comparison of the three methods for alpha 6 and 18 degrees are shown in Figure 21.

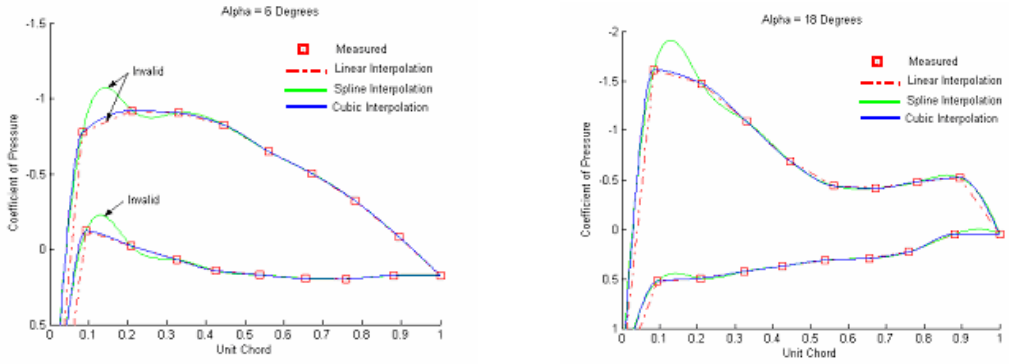

Figure 21: Coefficient of Pressure at 33 % Span

Knowing the C_l and ΔC_p values at various alphas, the airfoil constants *A* and *B* values were determined to be -0.11 and 0.75 respectively. The difference in C_l was less than a 2.4 percent between the approximation method and integration of the pressure coefficients for angles of attack less than 12 degrees and up to 10.3 percent above 12 degrees. This angle of attack is significant because it is in the region when the airfoil begins to stall and separation becomes a factor. Therefore, this method for approximating the local lift should only be applied to values less than $\alpha < 12$ degrees. A comparison between the integration of the pressure coefficients and the linear approximation are shown in Figure 22.

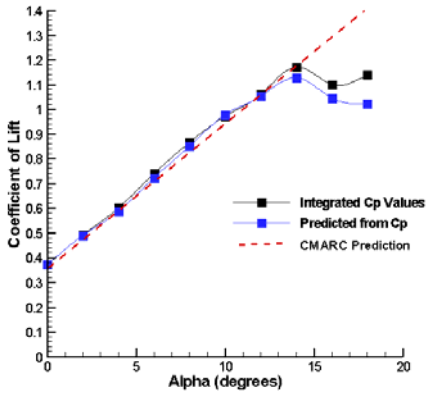

Figure 22: Comparison of Lift Coefficient Values at 33 % Span

Using the simple method for calculating the lift coefficient, the spanwise lift distribution was obtained for multiple angles of attack. The spanwise lift distribution correlated well between predicted and experimental values. The predicted distribution had a maximum error of 12.7% at an alpha of 0 degrees and 6.5 % at 10 degrees. The cause of the increase in the lift coefficient near the root at 0 degrees angle of attack was unable to be explained or attributed to viscous flow effects. A plot of the lift distribution is shown in Figure 23 below. Note again that port 44 produced invalid pressure.

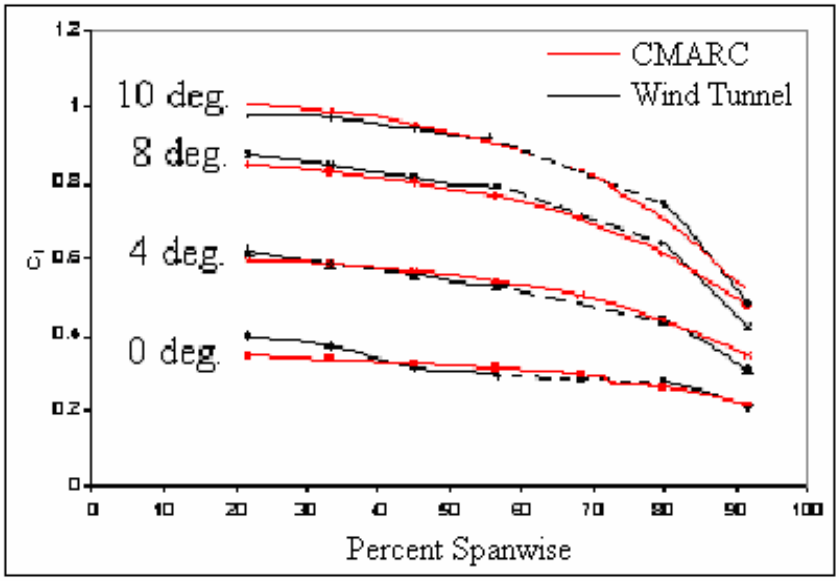

Figure 23: Spanwise Lift Distribution

4.4.3 Surface Flow Visualization

To aid in the analysis of the flow across the surface of the wing, tufts were attached with 1/256 in. thick tape on the upper surface of the wing. The tufts were spaced 1-1.5 in. apart in the spanwise direction and varied from 0.5-1.5 in. in the chordwise direction with lengths of 1-3 in. The flow visualizations were recorded using a hand held digital video

camcorder with 6.8 mega-pixels and a 22x optical zoom lens. Due to limited visibility of the wind tunnel model from directly above, images of the wing could only record partial span. The three primary states of flow observed in the surface flow visualization are shown in Figure 24.

Figure 24: Flow Condition Criteria for Tufts[19]

Using the above convention previously set by NASA during testing on the X-29, attached flow was defined as tufts in contact with the surface and showing limited motion. Unsteady flow was defined as tufts in contact with the surface and angled up to +/- 35 degrees. If the tuft arced above 35 degrees, it was taken that fluid in the boundary layer had lost the component of momentum that carried it across the surface in a direction perpendicular to the y-axis of wing. Therefore, if the tuft arced more than +/- 35 degrees, the flow was defined as separated.

Examining location and the state of flow verifies conclusions drawn from the pressure port data of this research. At a negative 6 degrees alpha, there is attached flow at the root and unsteady flow near the wing tips. Increasing the alpha results in a growing unsteady and separation of the flow at the root. At an alpha of 10 degrees, the flow at 33 % span begins to separate at 60 % chord. The chordwise redistribution at the root is due to turbulent separation resulting from the inward induced flow. Above an alpha of 12 degrees, root

separation occurs due to leading-edge separation, resulting in a loss of section lift. This separated flow directly correlates with the large differences between the wind tunnel data and CMARC pressure distributions.

Appendix 8.5 has multiple surface pictures, while Figure 25 and Figure 26 show the difference between low and high lift regions. The centers of the left and right figures are located at 80 and 33 percent span respectively.

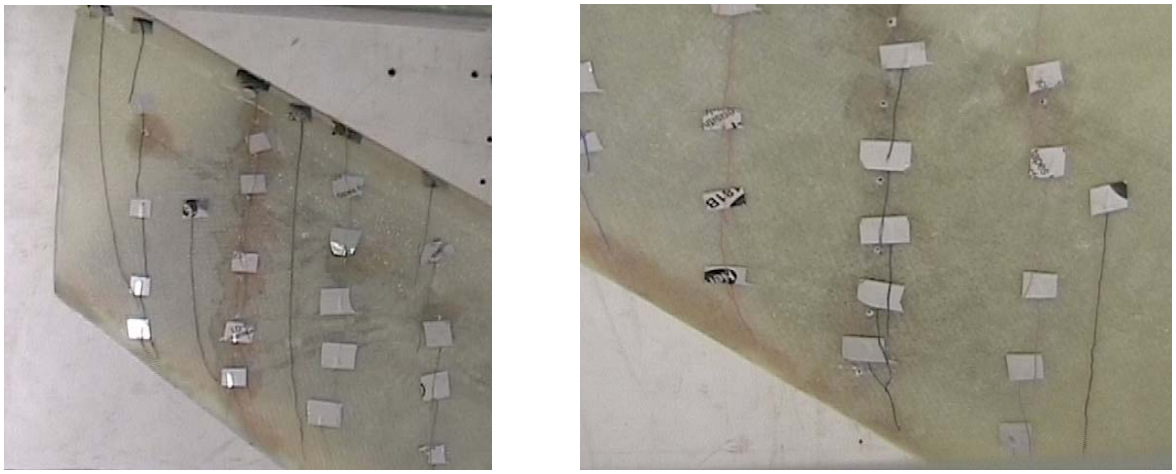

Figure 25: Flow Visualization on the Upper Surface at an Alpha of 0 Degrees

Figure 26: Flow Visualization on the Upper Surface at an Alpha of 10 Degrees

4.5 Conclusions

The general pressure distribution of the forward-swept wing was initially obtained by CMARC calculations. The viscous flow effects were then determined through the wind tunnel testing of a model with 52 pressure ports. It was concluded that the theoretical predictions of CMARC were limited to an alpha of 12 degrees. Above this angle of attack, it was necessary to use a more advanced aerodynamic analysis program or develop the distribution from the pressures obtained from the experimental testing. Since only two 16-port chordwise distributions were used on the pressure port wing, the precise pressure distribution was unable to be determined from the pressure plots. This occurred because the location and intensity of the chordwise pressures was unknown at locations other than 33 and 80 percent span. To enable the locations to be determined and increase the accuracy of the analysis, the number of chordwise pressure ports should be significantly increased with a large concentration of orifices near the trailing edge of the upper surface. However, the conclusions drawn from the pressure port data on separation and crossflow locations were verified through the tuft analysis. The prediction that the root separated at an alpha of 12 degrees and the flow remained attached at the wing tips above 18 degrees angle of attack was verified through the tuft analysis. Furthermore, the use of two pressure ports provided an accurate spanwise lift distribution prior to separation. The estimation of C_l using the two pressure ports and the CMARC pressure distribution were no longer valid once separation of the flow occurred at a C_l of 1.1.

5 STRUCTURES

5.1 Introduction

Forward-swept wings are often not a viable option because of the potential for aerodynamic and structural instabilities at high angles of attack. To avoid this, coupling between out of plane moments and deformations must be induced to overcome the airframe failure, resulting in an aeroelastically tailored wing.

The process to design a structurally tailored wing began by testing candidate materials. This allowed for accurate modeling of the material properties in the finite element analysis packages. Structural analysis was then performed in Unigraphics™ and ANSYS using aerodynamic loads predicted by CMARC. This consisted of performing numerous iterations by altering the placement of internal structures, layers of composite laminates, and fiber orientation of the skin. Upon completion of the structural design, the wing was constructed and instrumented with 9 strain gages. Ultimately, physical load and wind tunnel tests were performed to validate the ANSYS predictions.

5.2 Material Testing

Prior to designing the structures, the properties of candidate materials were obtained. Several coupons were tested to reduce errors resulting from flaws in the manufacturing and/or placement of the strain gages. To calculate the Modulus of Elasticity and Poisson's ratio, uniaxial strain gages in the 1st and 2nd principle axes were used. Testing in the Instron 4400 in Figure 27 was used to obtain these material properties.

Figure 27: The Instron 4400

The results of the testing are listed in Table 5-1 below.

Table 5-1: Candidate Material Properties

Material	Density (lb/in^3)	E_1 (Mpsi)	E_2 (Mpsi)	ν_{12}	ν_{21}
¾ oz Fiberglass*	0.031	0.339	0.339	0.22	0.22
2 oz Fiberglass*	0.062	2.760	2.760	0.12	0.12
Bi-Carbon*	0.064	8.680	5.280	0.20	0.12
Uni-Carbon*	0.040	12.88	0.786	0.17	0.01
1/8 in. Korex[20]	0.002	0.014	0.007	0.16	0.08
3/32 in. Balsa	0.006	0.523	0.065	0.23	0.02
Epoxy[21]	0.043	0.460	0.460	N/A	N/A

*Values obtained from coupons manufactured using West Systems Epoxy

Once the material properties were obtained, equation 3 was used to calculate the Shear Modulus.

$$G_{ij} = \frac{E_i}{2(1+\nu_{ij})} \qquad i,j = 1,2,3 \qquad (3)$$

In addition to the fundamental engineering constants used for input into ANSYS, ultimate strengths of each material were necessary for analyzing the point at which the structure fails.

Table 5-2: Material Failure Properties

	Tensile		Compressive	
Material	**σ_1 (ksi)**	**σ_2 (ksi)**	**σ_1 (ksi)**	**σ_2 (ksi)**
¾ oz Fiberglass*	17.0	17.0	6.20	6.20
2 oz Fiberglass*	30.0	30.0	11.0	11.0
Bi-Carbon*	60.0	30.0	13.3	6.70
Uni-Carbon*	65.0	0.45	13.8	0.08
1/8 in. Korex[20]	0.18	0.11	0.26	0.01
3/32 in. Balsa	10.6	0.14	1.20	0.18
Epoxy[21]	7.30	7.30	11.5	11.5

*Values obtained from coupons manufactured using West Systems Epoxy

5.3 Finite Element Model

The finite element analysis began with the creation of the model geometry and structural mesh in Unigraphics™. The process consisted of modeling the wing surface and internal structures in Unigraphics™ without the mounting points or voids in the lower wing surface. The rationale for the absence of these items is to increase the accuracy of the structural mesh and reduce computation time in the creation of the mesh and structural analysis. These model properties are critical for the representation of boundary conditions and were added during the refinement of the mesh in ANSYS. The distribution and shape of the elements is important to the accuracy of the structural analysis. The accuracy of the finite element analysis increases when elements are compact, without great elongation, skew, or warping[22]. The comparison between a model with and without the voids is shown in Figure 28 below. The voids are defined as geometric regions where the structure does not exist, such as bolt holes or opening for the wing mounts.

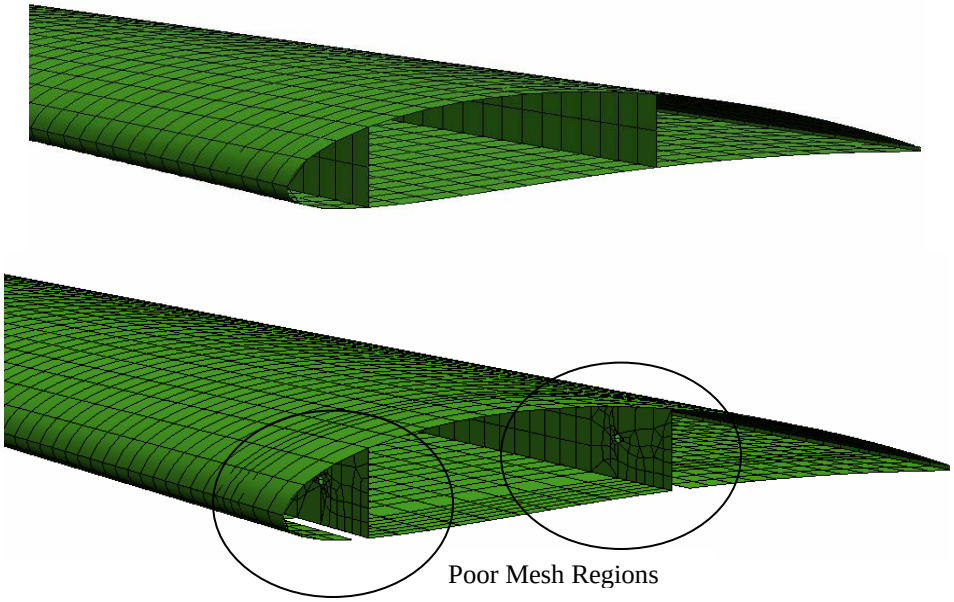

Figure 28: Structural Mesh Comparison

For equal element size, the mesh elements without the voids are less skewed, consistent in shape, orientation, and spanwise spacing. The elements around the location of the voids are refined in ANSYS to increase the density of the elements while maintaining consistent element shapes and sizes. To decrease the sensitivity of the element shape to deformation, the 8-node Shell 99 ANSYS element was used over the lower order elements. This reduces the shear locking effect that prohibits pure bending of the element. Even though these elements are less sensitive to shape distortion, there is still a distinct difference between the two strain distributions shown in Figure 29.

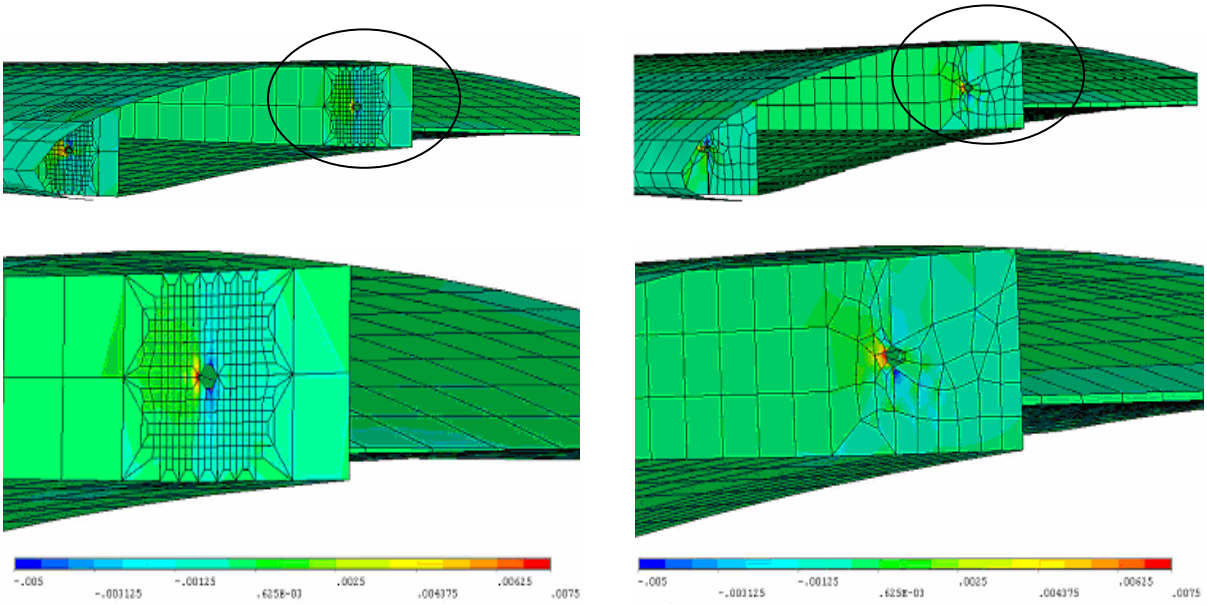

Figure 29: Varying YZ Shear Strain Due to Skewed Elements

It is obvious that the shape of the elements should remain as close to rectangular as possible to reduce the shear locking. In addition to the accuracy of the model, the fiber orientation is based on the local coordinate system of each element. Since orthotropic materials were used in the design, it is critical that the exact orientation angle of the material is known. If the elements do not have consistency, determining the angle of the material in the design and

manufacturing would be time consuming and varying throughout the structural components. For the elements of the model with the voids to become less skewed, the element size of the entire mesh would have to be greatly decreased. This reduction size exceeded the meshing capabilities of Unigraphics^{TM}, which produced invalid triangular and quadrilateral elements. Therefore, the model without the voids was refined in ANSYS to create the mount points and voids in the skin. The nodes and elements were written to a text file from Unigraphics^{TM}, which was loaded into ANSYS and used to merge the CMARC pressure distribution.

To simulate the interaction of the structures and mount points, boundary conditions were applied to the mesh. These restrict the degrees of freedom during the structural analysis. All degrees of freedom were restricted in ANSYS at the mount points while the transverse direction was fixed along the centerline.

5.4 ANSYS Simulations

Structural analysis performed in ANSYS consisted of performing numerous iterations by altering the placement of internal structures, layers of composite laminates, and fiber orientation of the skin. An overview of the iterative design process is shown in Figure 30.

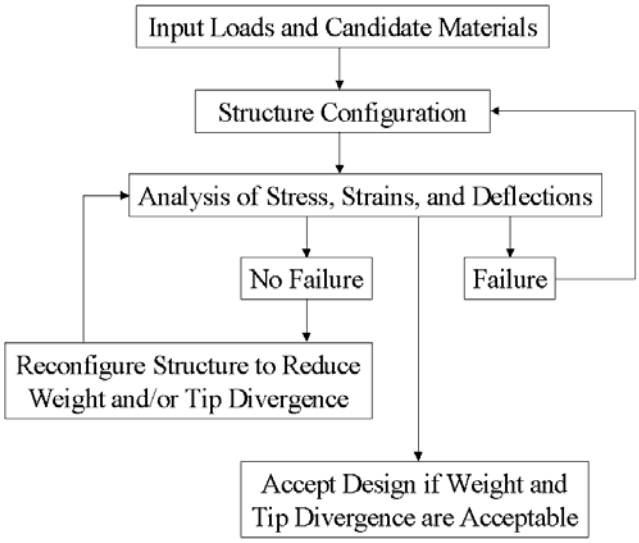

Figure 30: Structural Design Process

The design was deemed acceptable when another iteration of the structures would no longer reduce the wing tip twist without negatively impacting the safety factor of the structures. If the maximum stress in the structural components was not within 15 % of the failure stress with a 1.5 safety factor, the safety factor was considered compromised and the design was not accepted. Since the tailored wing was manufactured in-house, a restriction was imposed that limited the structural components to only one location in which the composite layers were altered. This reduces both the complexity in manufacturing and material discontinuities in the structures.

The finite element analysis performed in ANSYS took advantage of the linear layered Shell 99 element. This 8-node element allows for up to 250 composite layers to be modeled with varying thickness, orthotropic material properties, and material direction angles. This enabled numerous iterations of the composite properties without re-meshing or re-defining material properties of the structures.

The structural analysis used loads from CMARC at 0, 6, and 12 degrees angle of attack. The aerodynamic analysis in Chapter 4 demonstrated that the CMARC pressure distribution is accurate at angles of attack between 0 and 12 degrees; except between 50 and 90 percent chord, where the differences in pressures can be as much as 40 %. In this region, there is a decrease in suction on the upper surface of the pressure port wing that results in an increased nose up or leading edge up pitching moment. Again, this change in pressure distribution was not able to be accounted for in the finite element analysis due to uncertainty in the locations and intensity in which the reduction in lift occurs. Due to the fact that there were only two separate 16-port chordwise pressure distributions, it was observed that the reduction occurred at the root throughout the entire alpha range, while it did not exist at 80 % span above an alpha of 6 degrees. Furthermore, the decrease in pressure accounted for a C_l change less than 0.1 at 33 % span and 6 degrees angle of attack. In a worst-case scenario, if the C_L of the wing reduced by 0.1 at 6 degrees, it would change the lift of the wing by 2.1 lbs. or 14 % at the maximum dynamic pressure of the NCSU wind tunnel. Above an alpha of 12 degrees, separation at the root begins and the CMARC distribution is no longer considered to be valid. Again, the exact locations and intensity of the separation was unknown and could not be accounted for in the finite element analysis. To merge the CMARC pressure distribution and structural mesh, an in-house FORTRAN program was

used. The program utilizes a Gauss area interpolation to determine the coefficient of pressure for each node of the mesh. This pressure coefficient is used with other model parameters, such as wing area and C_L, to assign a pressure to each surface element of the mesh.

Once the boundary conditions and loads were applied to the structural mesh, the structural design began by performing numerous iterations to reduce weight and wing tip divergence. The initial design consisted solely of the wing skin without any internal structures. The composite material used in this analysis consisted of 4 layers of 2 oz. fiberglass with an 1/8 inch Korex core. This simulation enabled approximate locations of the spars/mount points to be determined by restricting all of the degrees of freedom at potential locations along the skin. The gold symbols in Figure 31 represent degrees of freedom that are locked, while the aqua symbols are degrees of freedom only restrained in the transverse direction.

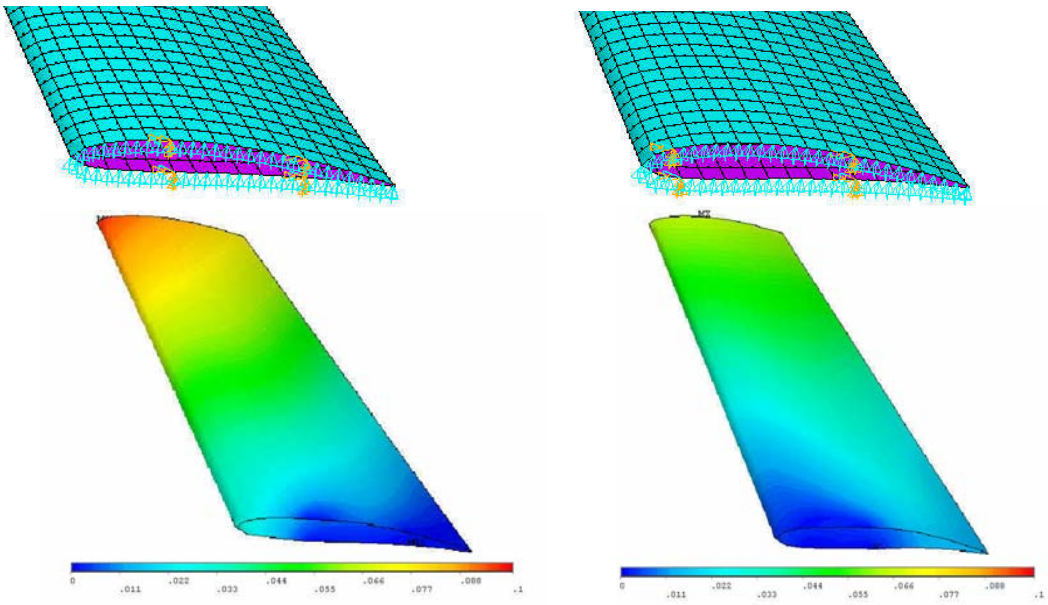

Figure 31: Determination of Spar Locations

The simulation indicated that the main mount point should be at the leading edge of the wing because as the main spar location moves farther aft, the tip deflection increases significantly. However, it is not feasible to position the main spar near the leading edge due to limitations imposed by the thickness of the airfoil at this location. Therefore, an initial location of 15 % chord was chosen as a compromise between the leading edge deflection and height of the main spar. The aft spar location was chosen such that the trailing edge of the root chord would deflect less than 0.03 inches, essentially no deflection. Therefore, initial spar locations were determined to be at 15 and 60 percent chord. Once the quantity and initial locations were established, the material layers and/or orientation of the composites were altered to increase the efficiency of the design. The final design consisted of a flexible aft spar and stiff main spar located at 13 and 58 percent chord respectively. The difference in stiffness allowed for an increase in the deflection of the trailing edge while reducing that of the leading edge. This was further amplified by composite skin that produced a coupling between the in-plane deformation and out-of-plane bending moment. This was accomplished by orienting the uni-directional carbon fiber between the spars at approximately 45 degrees with respect to the x-axis. This angle is approximately 15 degrees off of the quarter chord sweep angle, thus introducing an out of plane twist when the in-plane deformation occurs. Furthermore, to reduce the stresses and material discontinuities at the root, a 1.5 inch overlap of the fiber materials was used in the design.

The composite build-up for each component of the wing is listed in Table 5-3.

Table 5-3: Composite Build-Up

Description	Fiber*	Core Material
Main Spar	Bi-CF / 2 oz. FG	3/32 in. Balsa
Aft Spar	2 oz. FG / 2 oz. FG	3/32 in. Balsa
Wing Skin - Forward of Main Spar	¾ oz. FG / Bi-CF / 2 oz. FG	1/8 in. Korex
Wing Skin - Between Spars	¾ oz. FG / 2 oz. FG / Uni-CF	1/8 in. Korex
Wing Skin – Behind Aft Spar	¾ oz. FG / 2 oz. FG	1/8 in. Korex

*Composite layers are symmetric about the core material and do not include the 1.5 inch overlap

Using the component properties listed in Table 5-3, the maximum stress, deflection, and twist at the wing tip were obtained. These values are tabulated in Table 5-4 and the following figures show the deflection and stress distribution.

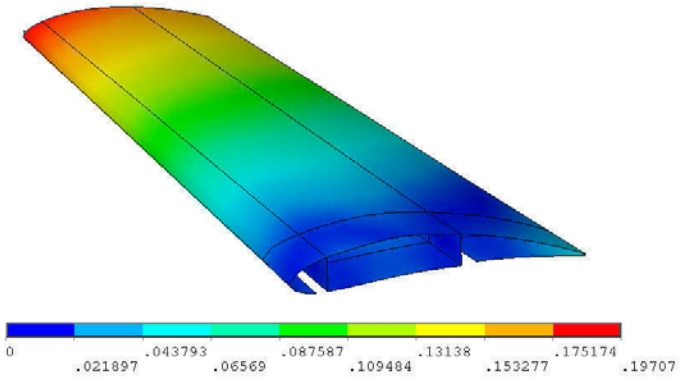

Figure 32: Deflection at an Alpha of 6 Degrees and Dynamic Pressure of 70 psf.

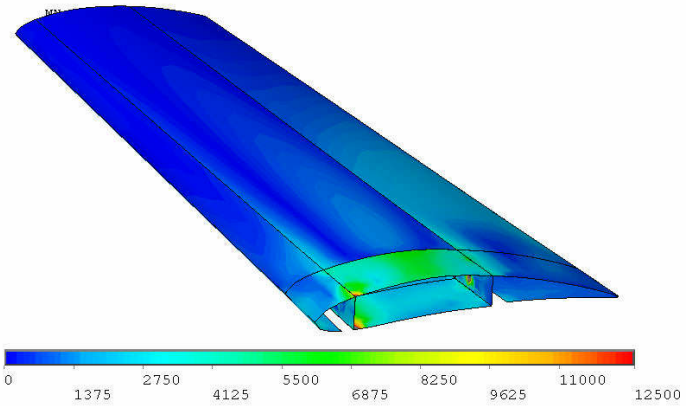

Figure 33: Stress at an Alpha of 6 Degrees and Dynamic Pressure of 70 psf.

Table 5-4: Wing Deformation and Stresses

Angle of Attack (deg.)	Dynamic Pressure* (psf.)	Maximum Stress (ksi.)	Maximum Deflection (in.)	Wing Tip Twist (deg.)
0	150	11.5	0.18	0.33
6	70	12.3	0.20	0.37
12	45	13.2	0.23	0.41

*Dynamic pressure is set to obtain a wing loading ratio of approximately 50 to 1

As expected, the wing tip twist increases with respect to the angle of attack. The predictions in maximum stress, deflection, and twist were approximately linear between 0 and 12 degrees. This occurred because the Shell 99 element used in ANSYS is linear and the CMARC pressure distribution can not model flow separation, and crossflow and separation modifications of the pressure distribution were unavailable. The maximum stress of 13.2 ksi. occurs at corner of the main spar and the skin at the root. The yielding stress of the composite at the joint is approximately 21.4 ksi., providing a safety factor of 1.6 in the region. Additional yield stresses and the associated safety factors for the final design are listed in Appendix 8.6. Although extensive design work went into completely eliminating the wing tip divergence, the tip twist was slightly positive. The design was deemed acceptable because the non-tailored wing twist was over 650 % that of the tailored wing structure. The non-tailored wing consisted of isotropic skin material and equal laminates for both spars. Therefore, the design process was concluded and manufacturing of the tailored wing began.

5.5 Manufacturing

To reduce airframe weight and increase the accuracy of the structural finite element analysis, special attention was necessary during the manufacturing of the tailored composite wing. In particular, the bond between the internal structures and skins, orientation of the fiber directions, and hard points for mounting.

5.5.1 Skins and Internal Structure

Upper and lower skins were manufactured using the molds previously manufactured. This ensured that the geometry of the tailored wing is almost identical to that of the previously tested pressure port wing. The manufacturing process began by cutting the fiber and core materials to the necessary dimensions. While the Korex core was one piece, the fiber included the additional layer of fiber on the opposing wing. For example, the fiber for the left wing included the 1.5 in. layer of the right wing at the root. This allowed for sufficient overlap of the bonded area, enabling loads to transfer through the joint. This eliminated geometry and material discontinuity at the ends of the bond material, which leads to a structural failure point.

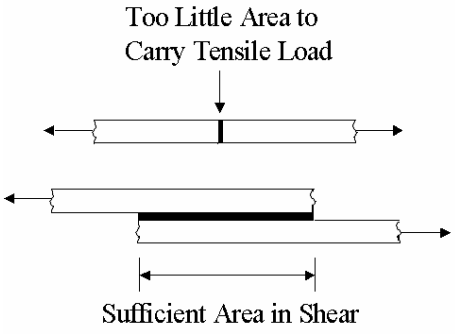

Figure 34: Good and Bad Load Transfer in Bonded Joints[3]

Prior to manufacturing the skins, locations of the spars and orientation of the uni-directional carbon fiber were labeled on the molds. The manufacturing of the skins consisted of the same wet lay-up, vacuum bag process that was used in the construction of the coupons previously tested.

Figure 35: Skin Manufacturing

Upon completion of the skins, excess material was removed and the internal structures were manufactured. The composite layers of each spar are listed in Table 5-5.

Table 5-5: Composite Layers for Internal Structures

	Main Spar	**Aft Spar**
Total Layers Design*	4.8 oz. Bi-Carbon Fiber 2.0 oz. Fiberglass 3/32 in. Balsa 2.0 oz. Fiberglass 4.8 oz. Bi-Carbon Fiber	2.0 oz. Fiberglass 2.0 oz. Fiberglass 3/32 in. Balsa 2.0 oz. Fiberglass 2.0 oz. Fiberglass
Manufactured Composite	2.0 oz. Fiberglass 3/32 in. Balsa 2.0 oz. Fiberglass	2.0 oz. Fiberglass 3/32 in. Balsa 2.0 oz. Fiberglass

*Composite layers do not include the 1.5 inch overlap

During the construction of the spars, a layer on each side of the composite was not included on the spars. This was intentionally done to allow for the layer of the spar and flange between the spars and skin to be constructed simultaneously. Similar to the overlapping layers on the skin, this increases the strength of the bond between the spar and the skin.

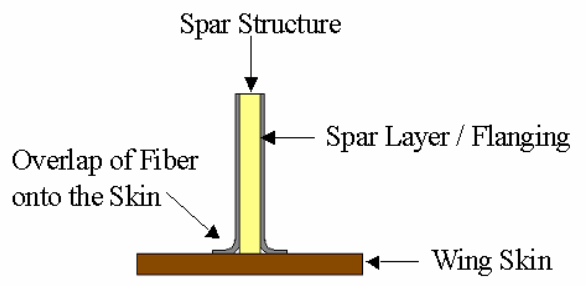

Figure 36: Flanging

Since the compressive strength of the core material is less than 200 psi., a hard point is necessary to ensure that the core will not crush when the mounting bolts are tightened. The hard point was constructed by removing a ½ in. diameter of the balsa core and a single layer of the fiberglass. The void was then filled with pure epoxy.

Figure 37: Hard Points

Following construction of the hard points, the structures were flanged to the skin with the appropriate layers.

5.5.2 Wing Mount

To interface the tailored wing to the wind tunnel balance and load testing stand, a 1/2 in. hard ply plate, 1/16 in. angled aluminum brackets, and assorted bolts and blind nuts were used. The brackets were set approximately 3/32 of an inch off of the spars to allow for the spar cap to be continuous across the wing. They were also angled parallel to the spars to enable the bolts holes to be perpendicular to the spar. The attached mounting plate is shown in Figure 38.

Figure 38: Installed Mounting Bracket

5.5.3 Strain Gages

To validate the predicted strain values obtained from ANSYS, stain gages were attached to the composite structures. A total of 9 gages were used; with 7 of the gages mounted internally. The gages were placed in low gradient regions with high strain values. It was also critical that multiple gages were placed on the main and trailing edge spars at various span locations to correlate the wing twist with strain values.

Furthermore, differences about the centerline and/or sensitivity of the gage placement are obtained by positioning gages on the left and right wing at the same location.

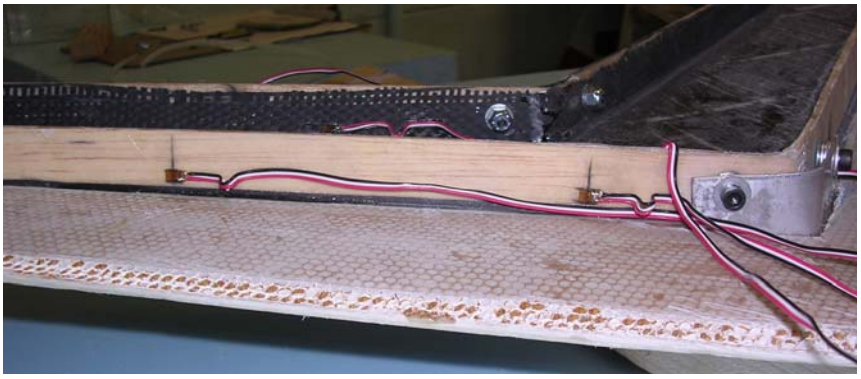

Figure 39: Internal Strain Gages

A brief description and location of each strain gage is listed in Table 5-6, while the coordinate locations are listed in Appendix 8.7.

Table 5-6: Strain Gage Location and Description

Gage Number	Description	% Span
1	Left Aft Spar, Back Side	13.9
2	Left Aft Spar, Back Side	41.7
3	Right Aft Spar, Back Side	13.9
4	Left Main Spar, Back Side	20.3
5	Left Main Spar, Front Side	20.3
6	Right Main Spar, Back Side	20.3
7	Left Main Spar, Back Side	43.5
8	Lower Skin, 0.25 in. off of Aft Spar, Parallel to Centerline	26.7
9	Lower Skin, Centered Between Spars, Parallel to Main Spar	16.7

Once the wing mount and internal strain gages were permanently installed, the upper and lower skins were joined together. Similar to the spars, layers were intentionally left off of the leading edge of the wing skins to allow for significant overlap through the joint. The joint consisted of a single layer of 4.8 oz. bi-carbon fiber and 0.75 oz. fiberglass. A mixture of epoxy and Kevlar pulp was used to join the trailing edges of the wing.

5.6 Structural Testing

To verify the ANSYS predictions, the tailored wing was subject to distributed point and aerodynamic loads. To prepare for these tests, test plans were written, the wing was mounted to the load test stand or balance, and weights were manufactured where needed.

5.6.1 Physical Load Testing

To verify the ANSYS predictions, special attention to the manufacturing in the previous section and testing of the tailored wing is necessary. Not only was the detail in construction of the wing vital, but similar flight-like loads and boundary conditions must also be applied to the test specimen. The boundary conditions for the wing were applied through bolts in the main and aft spars. Forces and moments for the physical testing were simulated with a distributed point load method.

Prior research on the Active Aeroelastic Wing F/A-18 structure showed that a 16-point chordwise distributed load provides significantly less error in the predicted strains when compared to a single point distributed load[23]. The chordwise loads were applied using 4 hydraulic cylinders with a whiffletree mechanism to distribute the loads to 4 different pads. This ideal apparatus for the physical testing of the tailored wing was unavailable and a single chordwise point load was used instead. Again, a test plan was followed to prevent catastrophic failure of the wing and/or damage to personnel. The first step of the test plan in Appendix 8.8 requires the manufacturing of the point loads or weights. These loads were generated as a result of sectioning the wing into panels and determining the associated weight for the section. To ease the placement of the weights on the wing, the number of columns per wing was determined to be 3. The load for each panel was calculated by integrating the

CMARC pressure coefficients to obtain the C_l and C_m for the associated wing panel. Dimensional forces and moments were then calculated by using panel area and a dynamic pressure of 10. The location of the load was then determined by translating the location of the lift force to produce the associated pitch and bending moment. The ANSYS model was not updated for these point loads due to the fact that the wind tunnel aerodynamics were being simulated and predicted and experimental strain values were compared. The locations and loads for 0, 6, and 12 degrees angle of attack are listed in Table 5-7 below.

Table 5-7: Load Distribution at a Dynamic Pressure of 10 psf.

Panel Number	Location (% Chord)	Location (% Span)	Single-point Load (lbs.)		
			α = 0 deg.	α = 6 deg.	α = 12 deg.
1	80	45	1.68	3.25	4.70
2	80	64	0.96	1.84	2.85
3	80	88	0.32	0.54	0.75

Once the weights were manufactured, the tailored wing was mounted to the rigid test stand and the physical load testing began, see Figure 40.

Figure 40: Load Test at a Simulated Alpha of 6 Degrees and q of 30 psf.

Upon completion of the test plan, data points for each angle of attack were obtained by averaging the data across each 3 second interval once the appropriate weights were placed on the wing. The strain data was then plotted against the simulated angle of attack. The ANSYS strain values were calculated by interpolating the 4 nearest surrounding nodes using the program in Appendix 8.9. The plots of gages not shown below are available in Appendix 8.10. The figures on the left correspond to 13.9 and 20.3 percent span, while the ones on the right are 41.7 and 43.5 percent span respectively.

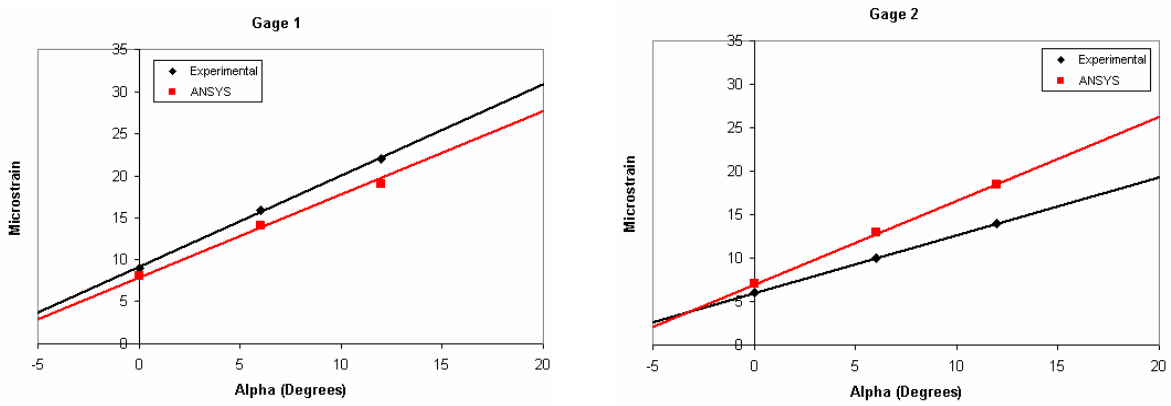

Figure 41: Aft Spar Strains

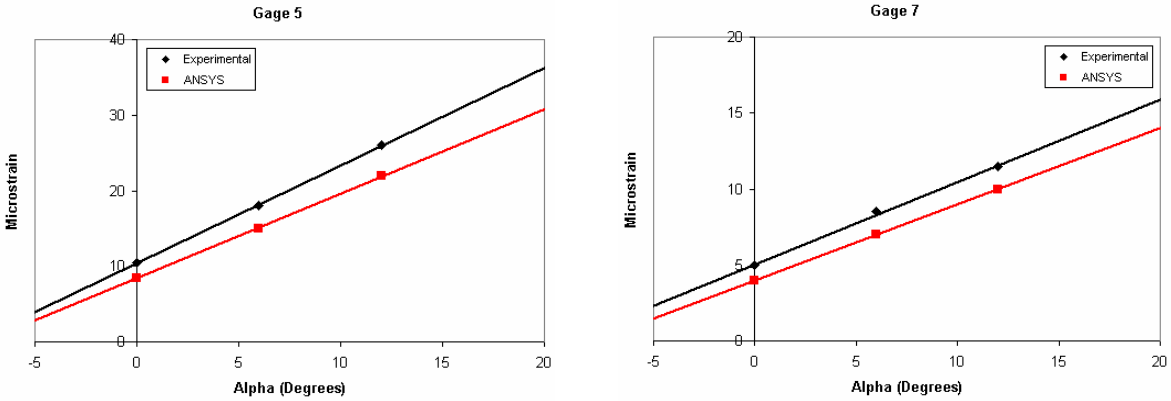

Figure 42: Main Spar Strains

As predicted, the slope of the strain with respect to angle of attack is linear. From this test, the correlation between predicted and experimental strain values had percent errors less than 33 % on 6 of the 9 gages and the test was deemed successful.

The strains from gages 4, 6, and 8 had errors ranging from 50 to 75 percent from predicted ANSYS strain values. Gages 4 and 6 were used to verify symmetry about the centerline and the strain values were within 15 % of each other.

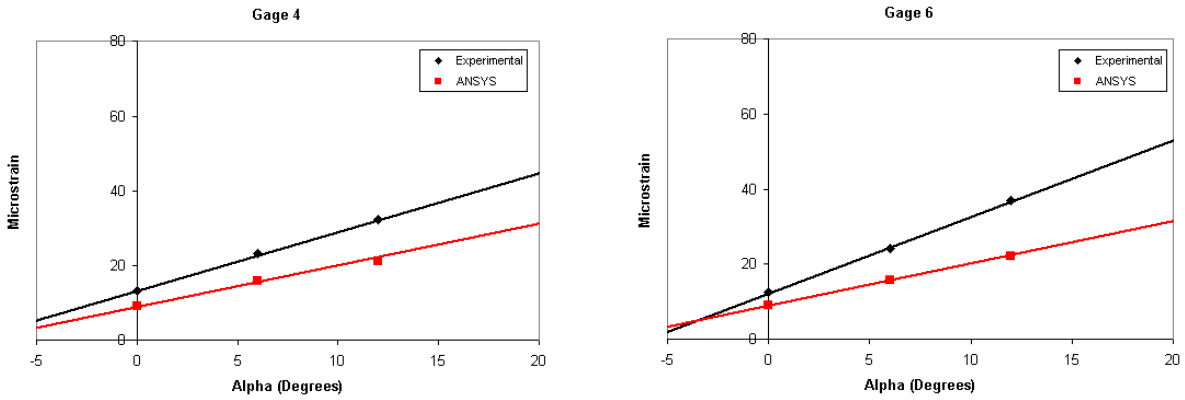

Figure 43: Strain Symmetry about Centerline

While the strains for gages 4 and 5 are significantly larger than predicted, they are similar in slope and magnitude as gage 5. This was important because gage 5 is in the same location as gage 4, but on the opposing side of the main spar. Therefore there was only a 25 % difference in strain between the two sides of the spar. This was important because it indicates that the main spar is experiencing almost pure bending and is not twisting. Gage 8 was located externally near the aft spar in the x-direction. The increase in strain in this region was likely due to the positioning of the strain gage. Although the other 8 gages were located in low gradient regions, to observe the compression of the wing skin, gage 8 was placed in the high gradient region between the aft and main spar. If the location of the gage was off by less then 1/16 of an inch, the strain value could vary +/- 15 %. The accuracy in

the placement of the strain gages on the spars was within 1/16 of an inch. For the placement of the external strain gages, the exact spar location was only known to 1/8 of an inch. Another source of error between predicted and experimental strain values could be the result of the joints which were not modeled in ANSYS. The ANSYS model assumes perfect joints and bonds between the composite layers and interaction between the skin and spars.

To safety qualify the tailored wing for the wind tunnel testing; an envelope expansion was conducted by increases the simulated dynamic pressure from 10 to 30 psf. in increments of 10 psf. This ensured that the wing would withstand aerodynamic loads much higher than those able to be achieved in the NCSU wind tunnel. Since the distributed load testing resulting in a linear strain slope, the envelope expansion consisted of loads only at a 6 degree angle off attack. From this test, it was proven that the wing is capable of withstanding a wing loading ratio of at 20 to 1. Although the wing was designed to a wing loading ration of 50 to 1, the test was halted at 20 to 1 to ensure that the wing was not damaged prior to the wind tunnel testing. The resulting strains are shown in Figure 44.

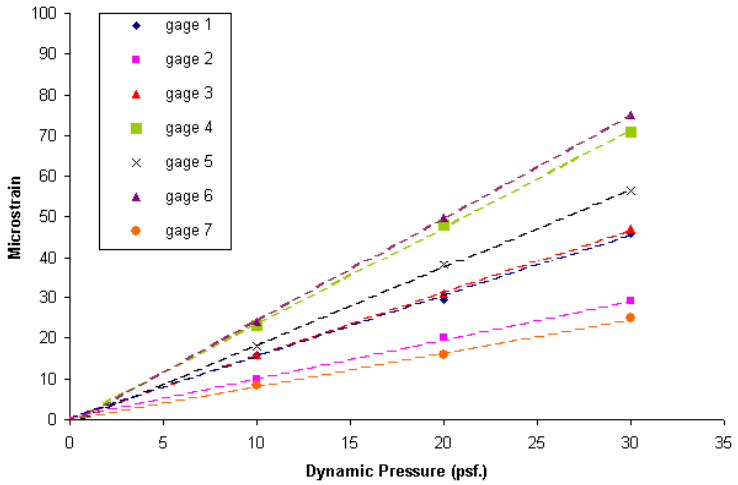

Figure 44: Envelope Expansion of Tailored Wing

The maximum strain for each gage during the wind tunnel test was typically less than 40 % of the proven capabilities of the wing. However, the maximum strain for gages 4 and 6 were within 15 % of safety qualified strain values. In addition to monitoring the strains during the envelope expansion, the leading and trailing edge deflections were measured at the wing tips. The deflections and corresponding wing twist angle are shown in Figure 45.

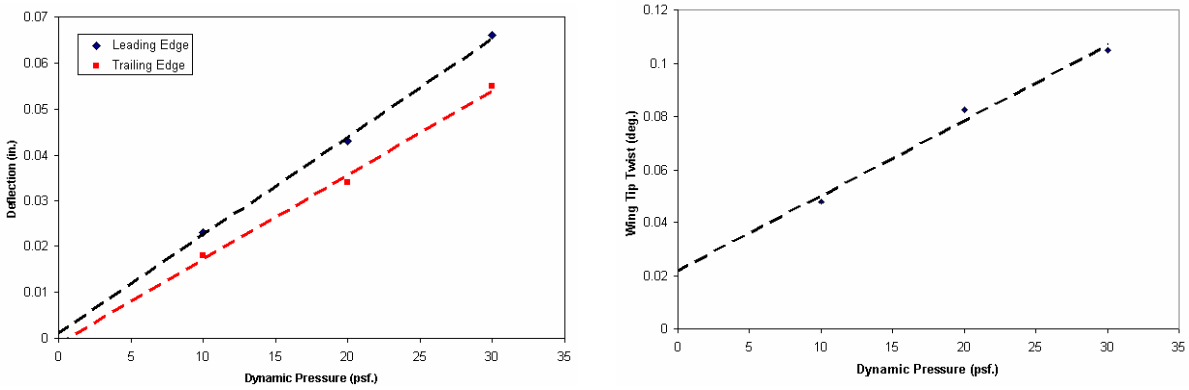

Figure 45: Wing Tip Deflection and Twist Angle

From the previous figures, it is clear that wing twist increases with respect to the dynamic pressure. This indicates amplification in the wing tip loading as dynamic pressure increases, thus resulting in the divergence phenomenon at the critical velocity. Using the data from the physical load test, it is estimated that the tailored wing experienced less than a 0.05 lb. increase in lift during the wind tunnel testing at 6 degrees angle of attack and a dynamic pressure of 10 psf.

5.6.2 Wind Tunnel Testing

Another alternative to verify the structural integrity of the wing structure is to test the wing under aerodynamic loads. Again, the appropriate loads must be applied to the wing under the boundary conditions modeled. The aerodynamic loads in this case were induced through testing the tailored wing in the NCSU subsonic wind tunnel at various angles of attack and dynamic pressures. The test plan in Appendix 8.11 was followed to prevent catastrophic failure of the wing and/or damage to the wind tunnel.

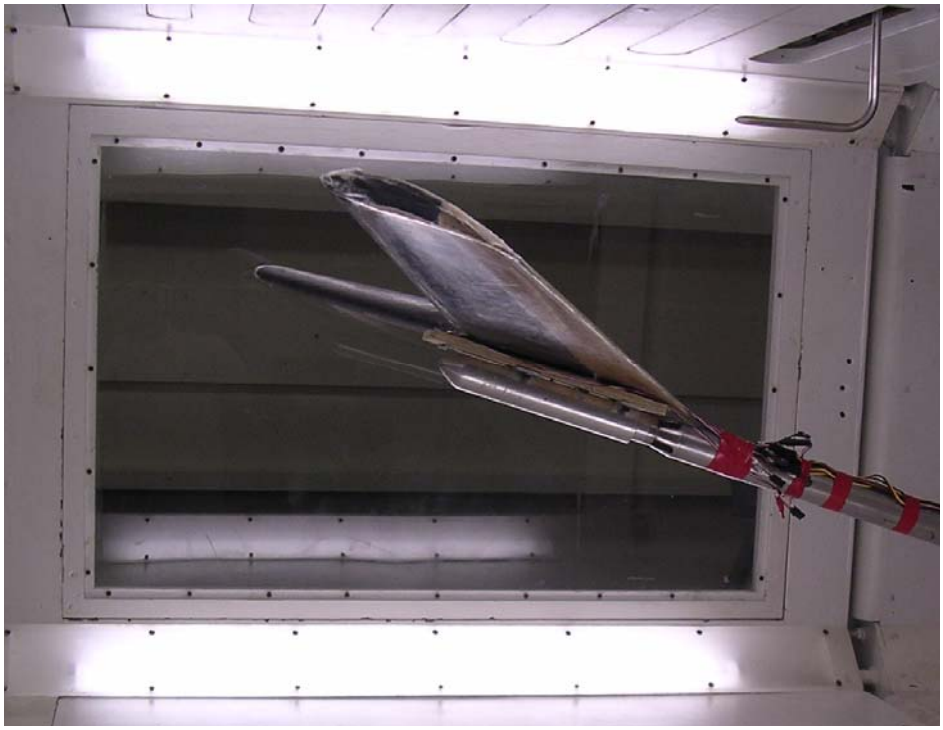

Figure 46: Wing Loading Test in the NCSU Wind Tunnel Testing

Upon completion of the test plan, data points for each angle of attack were obtained by averaging the data across each 3 second interval. The strain data was then plotted against the angle of attack. The plots of gages not shown below are available in Appendix 8.12. The figures on the left correspond to 13.9 and 20.3 percent span, while the ones on the right are 41.7 and 43.5 percent span respectively.

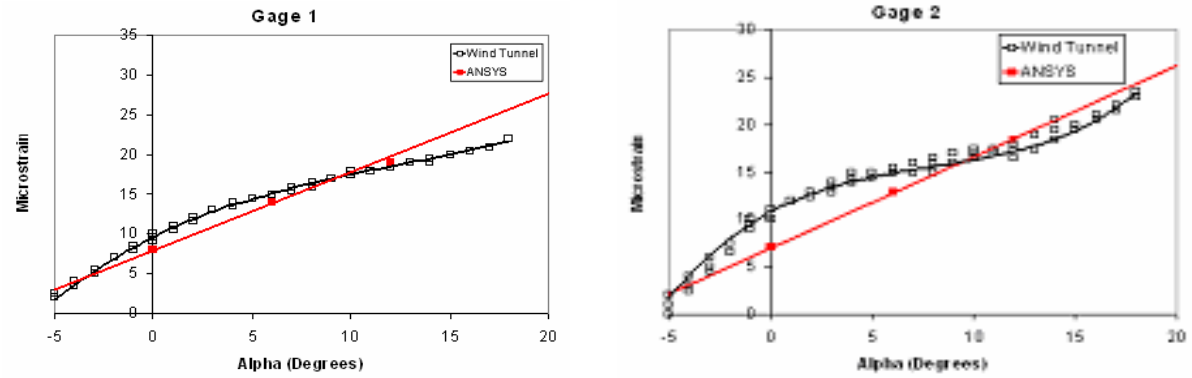

Figure 47: Aft Spar Strains

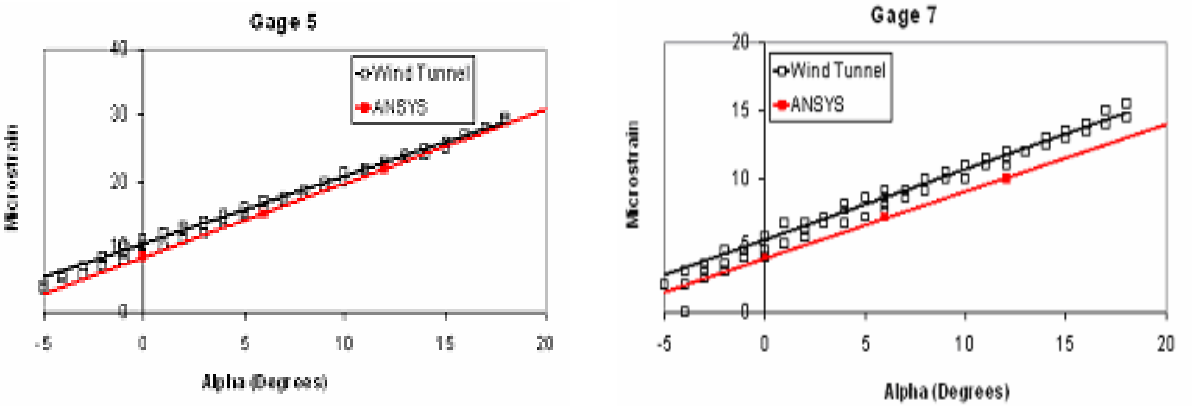

Figure 48: Main Spar Strains

The previous figures provide interesting results. The obvious conclusion was that the strain values of the main spar are linear while the aft spar was highly non-linear. This is significantly different from the physical load tests, where the slopes were linear for both

spars. The composite spar materials are linear in the low strain region; therefore the difference in linearity indicates a non-linear change in wing bending and/or pitching moment with respect to the angle of attack. Prior to 0 degrees alpha, the rate in which the strain increases in the aft spar was higher than predicted. The conclusion in this region was that the wing pitching and bending moment was lower than predicted. The strain rate in the aft spar greatly reduces between 2 and 8 degrees angle of attack. This directly correlates to the moderate lift region, where there is a chordwise redistribution in the pressure distribution that reduces the suction on the upper surface of the wing between 50 and 90 percent chord. In this region, the pitching moment increases and the strains approach the predicted values from ANSYS. Above an alpha of 12 degrees, the flow at 60 % root chord begins to separate, whereas the lift at the wing tip continues to increase. The shift in loading from the root to the wing tips results in an increasing the root bending and pitching moments. Overall, the correlation between predicted and experimental strains was exceptional, with differences in strain less than 33 % for 6 of the 9 gages.

The strains obtained by gages 4, 6, and 8 had errors ranging from 100 % to 150 % from predicted ANSYS strain values. Again, Gages 4 and 6 were used to verify symmetry about the centerline and the strain values were within 10 % of each other.

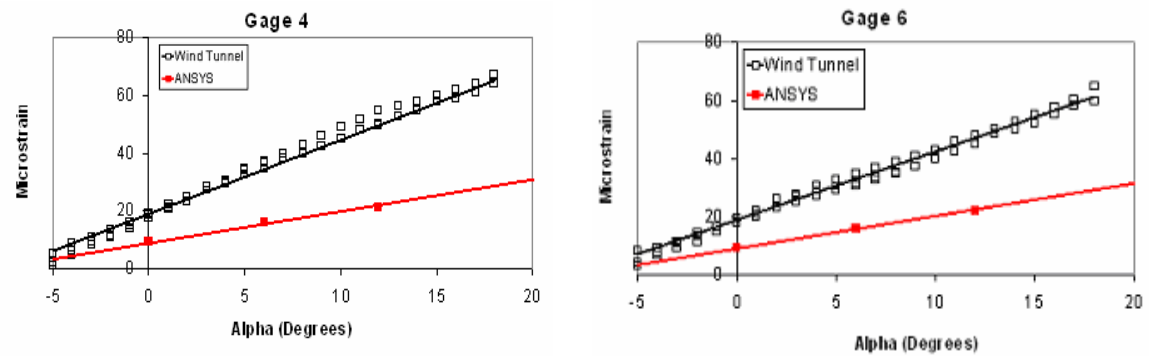

Figure 49: Strain Symmetry About the Wing Centerline

Although the strains were similar in slope and magnitude, they were much different than gage 5. Noting again that gage 5 was in the same location as gage 4, but on the opposing side of the main spar. Therefore there was a 117 % difference in strain between the two sides of the spar, which was much more than the physical testing and was not predicted in the structural analysis. The large difference between the opposing sides of the spar indicates that the spar was not in pure bending. The conclusion was that there was a slightly higher loading at the wing tips than anticipated from the aerodynamic analysis. A small increase in lift in this region would have significant increase in the root bending and pitching moment. Thus, explaining the increase of strain in gages 4 and 6 while decreasing the strain in gages 1 and 3. To ensure that delamination was not occurring, multiple wind tunnel tests were performed to duplicate the strain values previously obtained.

5.7 Conclusions

The structural design of the aeroelastically tailored wing resulted in an increase in the structural divergence velocity. This was accomplished by moving the elastic axis of the wing forward and exploiting the high stiffness-to-weight ratio of the composite materials in order to significantly reduce the wing tip twist. Although the structural design was not able to incorporate the effects of flow separation on the aerodynamic pressure distribution, the linear approximation of the strain was within 33 % of the experimental values for 6 out of 9 strain gages. The strain values also correlated well between the load tests with a distributed point load and wind tunnel tests. The wind tunnel testing did indicate that the aerodynamic loading at the wing tips was higher than was simulated by the load test or predicted by the aerodynamic analysis. This unexpected increase in force and moments significantly increased the strains at the root of the main spar; resulting in a reduction in the maximum aerodynamic loads the wing is capable of withstanding. From the wind tunnel tests, it was estimated that the wing was limited to a wing loading of 27 to 1 without exceeding the safety factor of the main spar.

6 CONCLUSIONS

This research again emphasizes the importance of accurate modeling of the aerodynamics and structural components during the design phase, in addition to the special attention necessary when manufacturing the test specimen. The aerodynamic analysis addressed the limitations of potential flow codes. The theoretical predictions of CMARC were limited to an alpha of 12 degrees. Due to an insufficient number of pressure ports, the precise modification to the CMARC aerodynamic model to depict the wind-tunnel-derived aerodynamics was unable to be determined. However, the conclusions drawn from the pressure port data were verified through the tuft analysis. Furthermore, the use of two pressure ports provided an accurate spanwise lift distribution prior to flow separation. Although the viscous flow effects were not included in the aerodynamic loads used for the structural analysis, the structural instabilities associated with the forward-swept wing were significantly reduced due to the aeroelastic tailoring of the wing structures. The strains also correlated well between ANSYS and the distributed point load and wind tunnel tests, with the strains for 6 out of 9 gages remaining within 33 percent of the predicted values.

7 REFERENCES

[1] Anderson, John D. Jr., *Introduction to Flight, fourth edition*, McGraw-Hill, Boston, MA, 2000.

[2] Dawson, Kenneth S. and Fortin, Paul E., "An Integrated Study of Structures, Aerodynamics, and Controls on the Forward-swept Wing X-29 and the Oblique Wing Research Aircraft," NASA-CR-181548, December 1987.

[3] Jones, Robert M., *Mechanics of Composite Materials, second edition*, Taylor and Francis, Philadelphia, PA, 1999.

[4] Sabbagh, Karl, *Twenty-first Century Jet*, Skyscrapers Production, Seattle, WA, 1995

[5] McCormack, Gerald M. and Cook, Woodrow L., "A Study of Stall Phenomena on a 45^{o} Swept-Forward Wing," NASA-TN-1797, January 1949.

[6] DeYoung, John, "Theoretical Additional Span Loading Characterisitcs of Wings with Arbitrary Sweep, Aspect Ratio, and Taper Ratio," NACA TN 1491, 1947.

[7] Ashby, Dale L. and Dudley, Michael R., "Potential Flow Theory and Operation Guide for the Panel Code PMARC," NASA Ames Research Center, July 1991.

[8] Duque, Earl P.M., Burklund, Michael D., and Johnson, Wayne, "Navier-Stokes and Comprehensive Analysis Performance Predictions of the NREL Phase VI Experiment," AIAA, 2003

[9] Schuster, Lawrence S. and Lokos William A., "Current Flight Test Experience Related to Structural Divergence of Forward-Swept Wings," NASA TM-100445, August 1988.

[10] Mercer, J.E. and Tinoco, E.N.,"FLEXSTAB: A Summary of the Functions and Capabilities of the NASA Flexible Airplane Analysis Computer System," NASA CR-2564, Decmber 1975.

[11] National Materials Advisory Board, *Computer-Aided Materials Selection During Structural Design*, Washington D.C., 1995

[12] Rae, William H. and Pope, Allen., *Low-Speed Wing Tunnel Testing, Second Edition,* John Wiley and Sons, New York, 1984.

[13] Gittner, N.M., An Investigation of the Effects of Aft Blowing on a 3.0 Caliber Tangent Ogive Body at High Angle of Attack, Master's Thesis, North Carolina State University, 1992.

[14] McComb, Harvey G., "Torsional Stiffness of Thin-Walled Shells Having Reinforcing Cores and Rectangular, Triangular, and Diamond Cross Section," NACA-TM-1316, January 1957.

[15] "ANSYS Release 9.0 Documentation – *Shell 99 Linear Layered Structural* Shell," ANSYS Inc., Canonsburg, PA, 2004.

[16] "Digital Wind Tunnel version 2.2 CMARC version 3.6 – *Three-Dimensional Low Order Panel Codes*," AeroLogic, 2000.

[17] Janiszewska, Jolanta M. and Lee, John D., "A Simple Method for Determining Lift and Drag on a Wing," Ohio State University.

[18] McAvoy, C.W., *Analytical and Experimental Approaches to Airfoil-Aircraft Design Integration*, Master's Thesis, North Carolina State University, 2002

[19] Del Frate, John H. and Saltzman, John A., "In-Flight Flow Visualization Results From the X-29A Aircraft at High Angles of Attack," NASA-TM-4430, November 1992.

[20] "Hexweb™ Honeycomb Attributes and Properties," Hexcel Composites, Pleasanton, CA, 2004.

[21] "Typical Physical Properties – West Systems Epoxy," Gougeon Brothers, Bay City, MI, 2000.

[22] Cook, Robert D., Malkus, David S., Plesha, Michael E., and Witt, Robert J., *Concepts and Applications of Finite Element Analysis, fourth edition*, John Wiley and Sons, Hoboken, NJ, 2002.

[23] Lokos, William A. and Stauf, Rick, "Strain-Gage Loads Calibration Parametric Study," NASA-TM-2004-212853, August 2004.

APPENDIX

8.1 CMARC Pressure Port Interpolation

```
PROGRAM Pressures_at_Ports

IMPLICIT NONE
real,DIMENSION(5,10000):: cmarc_coord !cmarc coords and pressures
REAL,DIMENSION(500,100,1000)::port_coord !closest points in cmarc
REAL,DIMENSION(500)::port_pres !avg pressure at port


real,DIMENSION(4,10000):: node_coord !ansys node coordinates
real,DIMENSION(5,10000):: final_data  !ansys coords and interpolated pressures
integer,DIMENSION(10,10000):: eset !ansys element-node definition

integer,DIMENSION(10000):: node_label !node labels
integer,DIMENSION(10000):: elem_label !element labels

real,DIMENSION(3,3)::plane_coord
integer:: axis

integer:: node_num     !number of ansys node points
integer:: elem_num     !number of ansys elements
integer:: aero_num     !number of cmarc panels

real   :: Cl     !Lift coefficielem_numt from cmarc
real::chord


CALL CMARC_read(cmarc_coord,aero_num,Cl,plane_coord,axis)
CALL PressPort_read(port_coord,cmarc_coord,port_pres)

CONTAINS

SUBROUTINE PressPort_read(port_coord,cmarc_coord,port_pres)

!-------------------------------------------------------------------------------
!This subroutine defines the four closest points around each port location
!           cmarc_coord = array of Cmarc pressure [x pos, y pos, z pos, Cp, above/below sep plane]
!-------------------------------------------------------------------------------

            IMPLICIT NONE
            REAL,INTENT(INOUT),DIMENSION(:,:)::cmarc_coord
            REAL,INTENT(INOUT),DIMENSION(:,:,:)::port_coord  !port number, 5=x location
            REAL,INTENT(INOUT),DIMENSION(:)::port_pres
            CHARACTER(50)::filename
            INTEGER:: i
            INTEGER:: ports
            REAL::LE12,LE5
            REAL::TE12,TE5
            REAL::d1,d2,d3
            REAL::k1,k2,k3,k4
            REAL::Cp12,Cp34,Cpavg(1000)
            REAL::c,chord
```

```
!User output of data file
        WRITE(*,*) ' Enter filelname for output data: '
        READ(*,*) filename
        OPEN(UNIT=50,file=filename,STATUS='unknown')

do i=1,4
port_coord(1,1,i)=cmarc_coord(i,3942)     port_coord(1,2,i)=cmarc_coord(i,3941)
port_coord(1,3,i)=cmarc_coord(i,4041)     port_coord(1,4,i)=cmarc_coord(i,4040)
port_coord(2,1,i)=cmarc_coord(i,3937)     port_coord(2,2,i)=cmarc_coord(i,3936)
port_coord(2,3,i)=cmarc_coord(i,4036)     port_coord(2,4,i)=cmarc_coord(i,4035)
port_coord(3,1,i)=cmarc_coord(i,3933)     port_coord(3,2,i)=cmarc_coord(i,3932)
port_coord(3,3,i)=cmarc_coord(i,4032)     port_coord(3,4,i)=cmarc_coord(i,4031)
port_coord(4,1,i)=cmarc_coord(i,3929)     port_coord(4,2,i)=cmarc_coord(i,3928)
port_coord(4,3,i)=cmarc_coord(i,4028)     port_coord(4,4,i)=cmarc_coord(i,4027)
port_coord(5,1,i)=cmarc_coord(i,3925)     port_coord(5,2,i)=cmarc_coord(i,3924)
port_coord(5,3,i)=cmarc_coord(i,4024)     port_coord(5,4,i)=cmarc_coord(i,4023)
port_coord(6,1,i)=cmarc_coord(i,3922)     port_coord(6,2,i)=cmarc_coord(i,3921)
port_coord(6,3,i)=cmarc_coord(i,4021)     port_coord(6,4,i)=cmarc_coord(i,4020)
port_coord(7,1,i)=cmarc_coord(i,3918)     port_coord(7,2,i)=cmarc_coord(i,3917)
port_coord(7,3,i)=cmarc_coord(i,4017)     port_coord(7,4,i)=cmarc_coord(i,4016)
port_coord(8,1,i)=cmarc_coord(i,3914)     port_coord(8,2,i)=cmarc_coord(i,3913)
port_coord(8,3,i)=cmarc_coord(i,4013)     port_coord(8,4,i)=cmarc_coord(i,4012)
port_coord(9,1,i)=cmarc_coord(i,3962)     port_coord(9,2,i)=cmarc_coord(i,3963)
port_coord(9,3,i)=cmarc_coord(i,4063)     port_coord(9,4,i)=cmarc_coord(i,4064)
port_coord(10,1,i)=cmarc_coord(i,3966)    port_coord(10,2,i)=cmarc_coord(i,3967)
port_coord(10,3,i)=cmarc_coord(i,4067)    port_coord(10,4,i)=cmarc_coord(i,4068)
port_coord(11,1,i)=cmarc_coord(i,3969)    port_coord(11,2,i)=cmarc_coord(i,3970)
port_coord(11,3,i)=cmarc_coord(i,4070)    port_coord(11,4,i)=cmarc_coord(i,4071)
port_coord(12,1,i)=cmarc_coord(i,3973)    port_coord(12,2,i)=cmarc_coord(i,3974)
port_coord(12,3,i)=cmarc_coord(i,4074)    port_coord(12,4,i)=cmarc_coord(i,4075)
port_coord(13,1,i)=cmarc_coord(i,3976)    port_coord(13,2,i)=cmarc_coord(i,3977)
port_coord(13,3,i)=cmarc_coord(i,4077)    port_coord(13,4,i)=cmarc_coord(i,4078)
port_coord(14,1,i)=cmarc_coord(i,3980)    port_coord(14,2,i)=cmarc_coord(i,3981)
port_coord(14,3,i)=cmarc_coord(i,4081)    port_coord(14,4,i)=cmarc_coord(i,4082)
port_coord(15,1,i)=cmarc_coord(i,3983)    port_coord(15,2,i)=cmarc_coord(i,3984)
port_coord(15,3,i)=cmarc_coord(i,4084)    port_coord(15,4,i)=cmarc_coord(i,4085)
port_coord(16,1,i)=cmarc_coord(i,3987)    port_coord(16,2,i)=cmarc_coord(i,3988)
port_coord(16,3,i)=cmarc_coord(i,4088)    port_coord(16,4,i)=cmarc_coord(i,4089)
port_coord(17,1,i)=cmarc_coord(i,4534)    port_coord(17,2,i)=cmarc_coord(i,4533)
port_coord(17,3,i)=cmarc_coord(i,4633)    port_coord(17,4,i)=cmarc_coord(i,4632)
port_coord(18,1,i)=cmarc_coord(i,3333)    port_coord(18,2,i)=cmarc_coord(i,3332)
port_coord(18,3,i)=cmarc_coord(i,3432)    port_coord(18,4,i)=cmarc_coord(i,3431)
port_coord(19,1,i)=cmarc_coord(i,2733)    port_coord(19,2,i)=cmarc_coord(i,2732)
port_coord(19,3,i)=cmarc_coord(i,2832)    port_coord(19,4,i)=cmarc_coord(i,2831)
port_coord(20,1,i)=cmarc_coord(i,2232)    port_coord(20,2,i)=cmarc_coord(i,2231)
port_coord(20,3,i)=cmarc_coord(i,2331)    port_coord(20,4,i)=cmarc_coord(i,2330)
port_coord(21,1,i)=cmarc_coord(i,1032)    port_coord(21,2,i)=cmarc_coord(i,1031)
port_coord(21,3,i)=cmarc_coord(i,1131)    port_coord(21,4,i)=cmarc_coord(i,1130)
port_coord(22,1,i)=cmarc_coord(i,1032)    port_coord(22,2,i)=cmarc_coord(i,1031)
port_coord(22,3,i)=cmarc_coord(i,1131)    port_coord(22,4,i)=cmarc_coord(i,1130)
port_coord(23,1,i)=cmarc_coord(i,2232)    port_coord(23,2,i)=cmarc_coord(i,2231)
port_coord(23,3,i)=cmarc_coord(i,2331)    port_coord(23,4,i)=cmarc_coord(i,2330)
port_coord(24,1,i)=cmarc_coord(i,2733)    port_coord(24,2,i)=cmarc_coord(i,2732)
```

port_coord(24,3,i)=cmarc_coord(i,2832) port_coord(24,4,i)=cmarc_coord(i,2831)
port_coord(25,1,i)=cmarc_coord(i,3333) port_coord(25,2,i)=cmarc_coord(i,3332)
port_coord(25,3,i)=cmarc_coord(i,3432) port_coord(25,4,i)=cmarc_coord(i,3431)
port_coord(26,1,i)=cmarc_coord(i,4534) port_coord(26,2,i)=cmarc_coord(i,4533)
port_coord(26,3,i)=cmarc_coord(i,4633) port_coord(26,4,i)=cmarc_coord(i,4632)
port_coord(27,1,i)=cmarc_coord(i,1640) port_coord(27,2,i)=cmarc_coord(i,1639)
port_coord(27,3,i)=cmarc_coord(i,1739) port_coord(27,4,i)=cmarc_coord(i,1738)
port_coord(28,1,i)=cmarc_coord(i,1635) port_coord(28,2,i)=cmarc_coord(i,1634)
port_coord(28,3,i)=cmarc_coord(i,1735) port_coord(28,4,i)=cmarc_coord(i,1734)
port_coord(29,1,i)=cmarc_coord(i,1631) port_coord(29,2,i)=cmarc_coord(i,1630)
port_coord(29,3,i)=cmarc_coord(i,1731) port_coord(29,4,i)=cmarc_coord(i,1730)
port_coord(30,1,i)=cmarc_coord(i,1628) port_coord(30,2,i)=cmarc_coord(i,1627)
port_coord(30,3,i)=cmarc_coord(i,1727) port_coord(30,4,i)=cmarc_coord(i,1726)
port_coord(31,1,i)=cmarc_coord(i,1625) port_coord(31,2,i)=cmarc_coord(i,1624)
port_coord(31,3,i)=cmarc_coord(i,1724) port_coord(31,4,i)=cmarc_coord(i,1723)
port_coord(32,1,i)=cmarc_coord(i,1621) port_coord(32,2,i)=cmarc_coord(i,1622)
port_coord(32,3,i)=cmarc_coord(i,1720) port_coord(32,4,i)=cmarc_coord(i,1719)
port_coord(33,1,i)=cmarc_coord(i,1617) port_coord(33,2,i)=cmarc_coord(i,1616)
port_coord(33,3,i)=cmarc_coord(i,1716) port_coord(33,4,i)=cmarc_coord(i,1715)
port_coord(34,1,i)=cmarc_coord(i,1612) port_coord(34,2,i)=cmarc_coord(i,1611)
port_coord(34,3,i)=cmarc_coord(i,1711) port_coord(34,4,i)=cmarc_coord(i,1710)
port_coord(35,1,i)=cmarc_coord(i,1661) port_coord(35,2,i)=cmarc_coord(i,1662)
port_coord(35,3,i)=cmarc_coord(i,1762) port_coord(35,4,i)=cmarc_coord(i,1763)
port_coord(36,1,i)=cmarc_coord(i,1666) port_coord(36,2,i)=cmarc_coord(i,1667)
port_coord(36,3,i)=cmarc_coord(i,1767) port_coord(36,4,i)=cmarc_coord(i,1768)
port_coord(37,1,i)=cmarc_coord(i,1670) port_coord(37,2,i)=cmarc_coord(i,1671)
port_coord(37,3,i)=cmarc_coord(i,1771) port_coord(37,4,i)=cmarc_coord(i,1772)
port_coord(38,1,i)=cmarc_coord(i,1674) port_coord(38,2,i)=cmarc_coord(i,1675)
port_coord(38,3,i)=cmarc_coord(i,1774) port_coord(38,4,i)=cmarc_coord(i,1775)
port_coord(39,1,i)=cmarc_coord(i,1677) port_coord(39,2,i)=cmarc_coord(i,1678)
port_coord(39,3,i)=cmarc_coord(i,1778) port_coord(39,4,i)=cmarc_coord(i,1779)
port_coord(40,1,i)=cmarc_coord(i,1681) port_coord(40,2,i)=cmarc_coord(i,1682)
port_coord(40,3,i)=cmarc_coord(i,1781) port_coord(40,4,i)=cmarc_coord(i,1782)
port_coord(41,1,i)=cmarc_coord(i,1684) port_coord(41,2,i)=cmarc_coord(i,1685)
port_coord(41,3,i)=cmarc_coord(i,1785) port_coord(41,4,i)=cmarc_coord(i,1786)
port_coord(42,1,i)=cmarc_coord(i,1689) port_coord(42,2,i)=cmarc_coord(i,1690)
port_coord(42,3,i)=cmarc_coord(i,1790) port_coord(42,4,i)=cmarc_coord(i,1791)
port_coord(43,1,i)=cmarc_coord(i,4569) port_coord(43,2,i)=cmarc_coord(i,4570)
port_coord(43,3,i)=cmarc_coord(i,4670) port_coord(43,4,i)=cmarc_coord(i,4671)
port_coord(44,1,i)=cmarc_coord(i,3369) port_coord(44,2,i)=cmarc_coord(i,3370)
port_coord(44,3,i)=cmarc_coord(i,3470) port_coord(44,4,i)=cmarc_coord(i,3471)
port_coord(45,1,i)=cmarc_coord(i,2769) port_coord(45,2,i)=cmarc_coord(i,2770)
port_coord(45,3,i)=cmarc_coord(i,2870) port_coord(45,4,i)=cmarc_coord(i,2871)
port_coord(401,1,i)=cmarc_coord(i,2270) port_coord(401,2,i)=cmarc_coord(i,2271)
port_coord(401,3,i)=cmarc_coord(i,2371) port_coord(401,4,i)=cmarc_coord(i,2372)
port_coord(402,1,i)=cmarc_coord(i,1070) port_coord(402,2,i)=cmarc_coord(i,1071)
port_coord(402,3,i)=cmarc_coord(i,1171) port_coord(402,4,i)=cmarc_coord(i,1172)
port_coord(403,1,i)=cmarc_coord(i,1070) port_coord(403,2,i)=cmarc_coord(i,1071)
port_coord(403,3,i)=cmarc_coord(i,1171) port_coord(403,4,i)=cmarc_coord(i,1172)
port_coord(404,1,i)=cmarc_coord(i,2270) port_coord(404,2,i)=cmarc_coord(i,2271)
port_coord(404,3,i)=cmarc_coord(i,2371) port_coord(404,4,i)=cmarc_coord(i,2372)
port_coord(405,1,i)=cmarc_coord(i,2769) port_coord(405,2,i)=cmarc_coord(i,2770)
port_coord(405,3,i)=cmarc_coord(i,2870) port_coord(405,4,i)=cmarc_coord(i,2871)
port_coord(406,1,i)=cmarc_coord(i,3369) port_coord(406,2,i)=cmarc_coord(i,3370)
port_coord(406,3,i)=cmarc_coord(i,3470) port_coord(406,4,i)=cmarc_coord(i,3471)

```
port_coord(457,1,i)=cmarc_coord(i,4569)    port_coord(457,2,i)=cmarc_coord(i,4570)
port_coord(457,3,i)=cmarc_coord(i,4670)    port_coord(457,4,i)=cmarc_coord(i,4671)
end do



!*********************************
!Port Coordinates
!*********************************
port_coord(1,5,1)=16.200          port_coord(1,5,2)=12.000          port_coord(1,5,3)=-1.320
port_coord(2,5,1)=16.960          port_coord(2,5,2)=12.000          port_coord(2,5,3)=-1.271
port_coord(3,5,1)=17.651          port_coord(3,5,2)=12.000          port_coord(3,5,3)=-1.179
port_coord(4,5,1)=18.520          port_coord(4,5,2)=12.000          port_coord(4,5,3)=-1.050
port_coord(5,5,1)=19.270          port_coord(5,5,2)=12.000          port_coord(5,5,3)=-0.946
port_coord(6,5,1)=20.030          port_coord(6,5,2)=12.000          port_coord(6,5,3)=-0.862
port_coord(7,5,1)=20.726          port_coord(7,5,2)=12.000          port_coord(7,5,3)=-0.808
port_coord(8,5,1)=21.580          port_coord(8,5,2)=12.000          port_coord(8,5,3)=-0.772
port_coord(9,5,1)=16.460          port_coord(9,5,2)=12.000          port_coord(9,5,3)=-0.447
port_coord(10,5,1)=17.130         port_coord(10,5,2)=12.000         port_coord(10,5,3)=-0.230
port_coord(11,5,1)=17.830         port_coord(11,5,2)=12.000         port_coord(11,5,3)=-0.101
port_coord(12,5,1)=18.680         port_coord(12,5,2)=12.000         port_coord(12,5,3)=-0.040
port_coord(13,5,1)=19.420         port_coord(13,5,2)=12.000         port_coord(13,5,3)=-0.061
port_coord(14,5,1)=20.140         port_coord(14,5,2)=12.000         port_coord(14,5,3)=-0.136
port_coord(15,5,1)=20.895         port_coord(15,5,2)=12.000         port_coord(15,5,3)=-0.271
port_coord(16,5,1)=21.540         port_coord(16,5,2)=12.000         port_coord(16,5,3)=-0.432
port_coord(27,5,1)=20.240         port_coord(27,5,2)= 5.000         port_coord(27,5,3)=-1.466
port_coord(28,5,1)=21.200         port_coord(28,5,2)= 5.000         port_coord(28,5,3)=-1.386
port_coord(29,5,1)=22.175         port_coord(29,5,2)= 5.000         port_coord(29,5,3)=-1.250
port_coord(30,5,1)=23.010         port_coord(30,5,2)= 5.000         port_coord(30,5,3)=-1.126
port_coord(31,5,1)=23.950         port_coord(31,5,2)= 5.000         port_coord(31,5,3)=-0.997
port_coord(32,5,1)=24.936         port_coord(32,5,2)= 5.000         port_coord(32,5,3)=-0.893
port_coord(33,5,1)=25.816         port_coord(33,5,2)= 5.000         port_coord(33,5,3)=-0.827
port_coord(34,5,1)=26.831         port_coord(34,5,2)= 5.000         port_coord(34,5,3)=-0.787
port_coord(35,5,1)=20.164         port_coord(35,5,2)= 5.000         port_coord(35,5,3)=-0.443
port_coord(36,5,1)=21.230         port_coord(36,5,2)= 5.000         port_coord(36,5,3)=-0.095
port_coord(37,5,1)=22.220         port_coord(37,5,2)= 5.000         port_coord(37,5,3)= 0.072
port_coord(38,5,1)=23.190         port_coord(38,5,2)= 5.000         port_coord(38,5,3)= 0.124
port_coord(39,5,1)=24.150         port_coord(39,5,2)= 5.000         port_coord(39,5,3)= 0.089
port_coord(40,5,1)=25.075         port_coord(40,5,2)= 5.000         port_coord(40,5,3)=-0.009
port_coord(41,5,1)=26.005         port_coord(41,5,2)= 5.000         port_coord(41,5,3)=-0.190
port_coord(42,5,1)=26.940         port_coord(42,5,2)= 5.000         port_coord(42,5,3)=-0.435



!User input of ports being used
Write(*,*)"Select Ports which are being used"
Write(*,*)"1 = Ports 1-16"
Write(*,*)"2 = Ports 27-42"
Read(*,*)ports
If(ports ==1)Then
        LE12 = 15.700     !assuming large postive pressure
```

```
        TE12 = 22.420   !assuming same pressure as port 8
        chord = TE12-LE12
        Write(50,*)0,1.5
Do i=1,8
        d1 = sqrt(  (port_coord(i,1,1)-port_coord(i,2,1))**2.0  +  0.0**2.0  +  (port_coord(i,1,3)-
port_coord(i,2,3))**2.0  )
        k1 = sqrt(  (port_coord(i,1,1)-port_coord(i,5,1))**2.0  +  0.0**2.0  +  (port_coord(i,1,3)-
port_coord(i,5,3))**2.0  )
        k2=d1-k1
        Cp12 = (port_coord(i,1,4)*k1+port_coord(i,2,4)*k2)/d1

        d2 = sqrt(  (port_coord(i,3,1)-port_coord(i,4,1))**2.0  +  0.0**2.0  +  (port_coord(i,3,3)-
port_coord(i,4,3))**2.0  )
        k1 = sqrt(  (port_coord(i,3,1)-port_coord(i,5,1))**2.0  +  0.0**2.0  +  (port_coord(i,3,3)-
port_coord(i,5,3))**2.0  )
        k2=d2-k1
        Cp34 = (port_coord(i,3,4)*k1+port_coord(i,4,4)*k2)/d2
        d3 = sqrt(   0.0**2.0  +  (port_coord(i,1,2)-port_coord(i,3,2))**2.0  +  (port_coord(i,1,3)-
port_coord(i,3,3))**2.0 )
        k3 = sqrt(   0.0**2.0  +  (port_coord(i,1,2)-port_coord(i,5,2))**2.0  +  (port_coord(i,1,3)-
port_coord(i,5,3))**2.0 )
        k4=d3-k3
        Cpavg(i) = (Cp12*k3+Cp34*k4)/d3
        write(50,*)(port_coord(i,5,1)-LE12)/chord,Cpavg(i)
        End Do
        Write(50,*)1,Cpavg(8)
        Write(50,*)1,Cpavg(8)
        Do i=1,8
        d1 = sqrt(  (port_coord(17-i,1,1)-port_coord(17-i,2,1))**2.0  +  0.0**2.0  +  (port_coord(17-i,1,3)-
port_coord(17-i,2,3))**2.0  )
        k1 = sqrt(  (port_coord(17-i,1,1)-port_coord(17-i,5,1))**2.0  +  0.0**2.0  +  (port_coord(17-i,1,3)-
port_coord(17-i,5,3))**2.0  )
        k2=d1-k1
        Cp12 = (port_coord(17-i,1,4)*k1+port_coord(17-i,2,4)*k2)/d1

        d2 = sqrt(  (port_coord(17-i,3,1)-port_coord(17-i,4,1))**2.0  +  0.0**2.0  +  (port_coord(17-i,3,3)-
port_coord(17-i,4,3))**2.0  )
        k1 = sqrt(  (port_coord(17-i,3,1)-port_coord(17-i,5,1))**2.0  +  0.0**2.0  +  (port_coord(17-i,3,3)-
port_coord(17-i,5,3))**2.0  )
        k2=d2-k1
        Cp34 = (port_coord(17-i,3,4)*k1+port_coord(17-i,4,4)*k2)/d2
        d3 = sqrt(   0.0**2.0  +  (port_coord(17-i,1,2)-port_coord(17-i,3,2))**2.0  +  (port_coord(17-i,1,3)-
port_coord(17-i,3,3))**2.0 )
        k3 = sqrt(   0.0**2.0  +  (port_coord(17-i,1,2)-port_coord(17-i,5,2))**2.0  +  (port_coord(17-i,1,3)-
port_coord(17-i,5,3))**2.0 )
        k4=d3-k3
        Cpavg(17-i) = (Cp12*k3+Cp34*k4)/d3
        write(50,*)(port_coord(17-i,5,1)-LE12)/chord,Cpavg(17-i)
        End Do
        Write(50,*)0,1.5

Else If(ports == 2)Then
        LE5 = 19.458      !assuming large postive pressure
        TE5 = 27.820   !assuming same pressure as port 34
        chord = TE5-LE5
```

```
        Write(50,*)0,1.5
        Do i=27,34
        d1 = sqrt(  (port_coord(i,1,1)-port_coord(i,2,1))**2.0  +  0.0**2.0  +  (port_coord(i,1,3)-
port_coord(i,2,3))**2.0  )
        k1 = sqrt(  (port_coord(i,1,1)-port_coord(i,5,1))**2.0  +  0.0**2.0  +  (port_coord(i,1,3)-
port_coord(i,5,3))**2.0  )
        k2=d1-k1
        Cp12 = (port_coord(i,1,4)*k1+port_coord(i,2,4)*k2)/d1
        d2 = sqrt(  (port_coord(i,3,1)-port_coord(i,4,1))**2.0  +  0.0**2.0  +  (port_coord(i,3,3)-
port_coord(i,4,3))**2.0  )
        k1 = sqrt(  (port_coord(i,3,1)-port_coord(i,5,1))**2.0  +  0.0**2.0  +  (port_coord(i,3,3)-
port_coord(i,5,3))**2.0  )
        k2=d2-k1
        Cp34 = (port_coord(i,3,4)*k1+port_coord(i,4,4)*k2)/d2
        d3 = sqrt(   0.0**2.0  +  (port_coord(i,1,2)-port_coord(i,3,2))**2.0  +  (port_coord(i,1,3)-
port_coord(i,3,3))**2.0 )
        k3 = sqrt(   0.0**2.0  +  (port_coord(i,1,2)-port_coord(i,5,2))**2.0  +  (port_coord(i,1,3)-
port_coord(i,5,3))**2.0 )
        k4=d3-k3
        Cpavg(i) = (Cp12*k3+Cp34*k4)/d3
        write(50,*)(port_coord(i,5,1)-LE5)/chord,Cpavg(i)
        End Do
        Write(50,*)1,Cpavg(34)
        Write(50,*)1,Cpavg(34)
        Do i=1,8
        d1 = sqrt(  (port_coord(43-i,1,1)-port_coord(43-i,2,1))**2.0  +  0.0**2.0  +  (port_coord(43-i,1,3)-
port_coord(43-i,2,3))**2.0  )
        k1 = sqrt(  (port_coord(43-i,1,1)-port_coord(43-i,5,1))**2.0  +  0.0**2.0  +  (port_coord(43-i,1,3)-
port_coord(43-i,5,3))**2.0  )
        k2=d1-k1
        Cp12 = (port_coord(43-i,1,4)*k1+port_coord(43-i,2,4)*k2)/d1
        d2 = sqrt(  (port_coord(43-i,3,1)-port_coord(43-i,4,1))**2.0  +  0.0**2.0  +  (port_coord(43-i,3,3)-
port_coord(43-i,4,3))**2.0  )
        k1 = sqrt(  (port_coord(43-i,3,1)-port_coord(43-i,5,1))**2.0  +  0.0**2.0  +  (port_coord(43-i,3,3)-
port_coord(43-i,5,3))**2.0  )
        k2=d2-k1
        Cp34 = (port_coord(43-i,3,4)*k1+port_coord(43-i,4,4)*k2)/d2
        d3 = sqrt(   0.0**2.0  +  (port_coord(43-i,1,2)-port_coord(43-i,3,2))**2.0  +  (port_coord(43-i,1,3)-
port_coord(43-i,3,3))**2.0 )
        k3 = sqrt(   0.0**2.0  +  (port_coord(43-i,1,2)-port_coord(43-i,5,2))**2.0  +  (port_coord(43-i,1,3)-
port_coord(43-i,5,3))**2.0 )
        k4=d3-k3
        Cpavg(43-i) = (Cp12*k3+Cp34*k4)/d3
        write(50,*)(port_coord(43-i,5,1)-LE5)/chord,Cpavg(43-i)
        End Do
        Write(50,*)0,1.5
End if
END SUBROUTINE PressPort_read
```

```
*******************************************************************************
SUBROUTINE CMARC_read(cmarc_coord,panel,CL,plane_coord,axis)
!------------------------------------------------------------------------------
!This subroutine reads Cmarc data and puts it into an array
!The Cmarc data must be unmodified and all spacing in the file
!must be as originally created by Cmarc.
!           cmarc_coord = array of Cmarc pressure [x pos, y pos, z pos, Cp, above/below sep plane]
!           panel      = number of Cmarc panels
!------------------------------------------------------------------------------
           IMPLICIT NONE
           REAL,INTENT(INOUT),DIMENSION(:,:)::cmarc_coord
           INTEGER,INTENT(INOUT)::panel
           REAL,INTENT(INOUT) :: Cl
           REAL,INTENT(INOUT),DIMENSION(:,:)::Plane_coord
           INTEGER, INTENT(IN):: axis
           CHARACTER(50)::filename
           CHARACTER(60)::temp
           INTEGER::above
           INTEGER:: i
           INTEGER:: counter
           INTEGER:: step
!User input of data file
           WRITE(*,*) ' Enter filelname for Cmarc data: '
           READ(*,*) filename
           OPEN(UNIT=45,file=filename,STATUS='unknown')
           counter = 0
           DO
                      read(45,'(A50)') temp
                      IF (temp(2:6) =='PANEL') THEN
                                 read(45,'(A1)') temp
                                 step = 1
                                 DO
                                 counter = counter + 1
                                            READ(45,*)
panel,cmarc_coord(1,panel),cmarc_coord(2,panel),cmarc_coord(3,panel),cmarc_coord(4,panel)
                                            read(45,'(A7)') temp
                                            IF (temp == '') THEN                    !found the end of a sequence of panels
                                                       counter = counter - 1
                                                       EXIT
                                            END IF
                                            BACKSPACE(45)
                                 END DO
                      ELSE IF (temp(31:45) =='TOTAL COEFFICIE') THEN
                                 read(45,'(A1)') temp
                                 read(45,'(A1)') temp
                                 read(45,'(A1)') temp
                                 read(45,'(A45)') temp
                                 read(temp(35:40),*) Cl
                                 write(*,*) 'Cl (from Cmarc) = ',Cl
                                 EXIT
                      END IF
           END DO
END SUBROUTINE CMARC_read
END Program
```

8.2 Pressure Port Location

Port Number	Surface	% Chord	% Span
1	Lower	7.4	80.0
2	Lower	18.7	80.0
3	Lower	29.1	80.0
4	Lower	42.0	80.0
5	Lower	53.1	80.0
6	Lower	64.4	80.0
7	Lower	74.8	80.0
8	Lower	87.5	80.0
9	Upper	11.3	80.0
10	Upper	21.3	80.0
11	Upper	31.7	80.0
12	Upper	44.3	80.0
13	Upper	55.4	80.0
14	Upper	66.1	80.0
15	Upper	77.3	80.0
16	Upper	86.9	80.0
17	Lower	33.0	91.7
18	Lower	33.0	68.3
19	Lower	33.0	56.7
20	Lower	33.0	45.0
21	Lower	33.0	21.7
22	Lower	33.0	21.7
23	Lower	33.0	45.0
24	Lower	33.0	56.7
25	Lower	33.0	68.3

26	Lower	33.0	91.7
27	Lower	9.4	33.3
28	Lower	20.8	33.3
29	Lower	32.5	33.3
30	Lower	42.5	33.3
31	Lower	53.7	33.3
32	Lower	65.5	33.3
33	Lower	76.0	33.3
34	Lower	88.2	33.3
35	Upper	8.4	33.3
36	Upper	21.2	33.3
37	Upper	33.0	33.3
38	Upper	44.6	33.3
39	Upper	56.1	33.3
40	Upper	67.1	33.3
41	Upper	78.3	33.3
42	Upper	89.5	33.3
43	Upper	33.0	91.7
44	Upper	33.0	68.3
45	Upper	33.0	56.7
401*, “46”	Upper	33.0	45.0
402*, “47”	Upper	33.0	21.7
403*, “48”	Upper	33.0	21.7
404*, “49”	Upper	33.0	45.0
405*, “50”	Upper	33.0	56.7
406*, “51”	Upper	33.0	68.3
457*, “52"	Upper	33.0	91.7

*Port numbering above 45 was a combination of labels less than 45

8.3 Pressure Plots

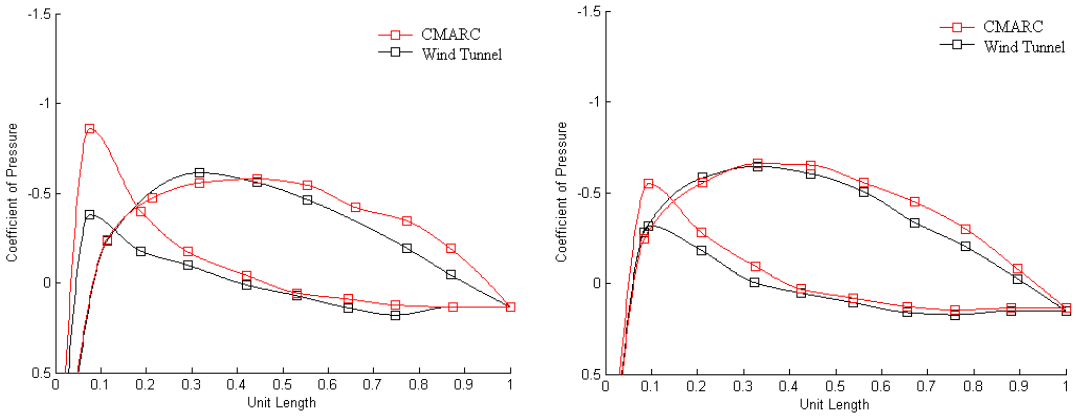

Alpha = 0 Degrees

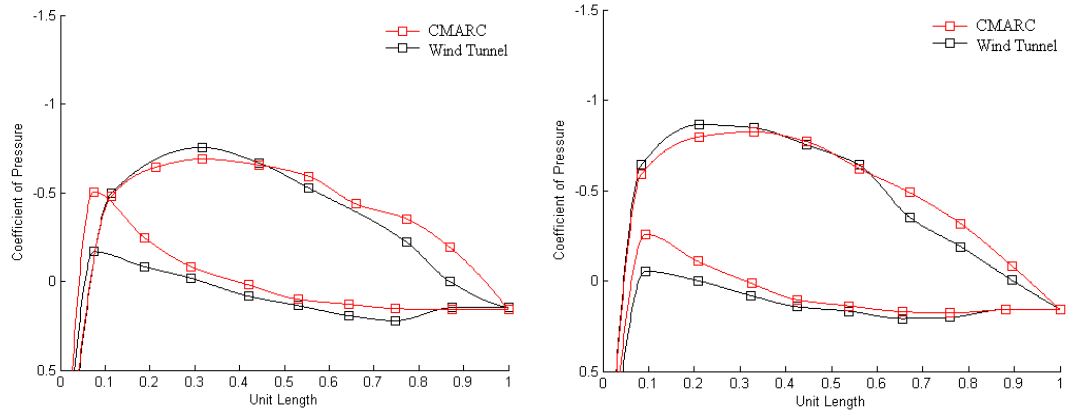

Alpha = 4 Degrees

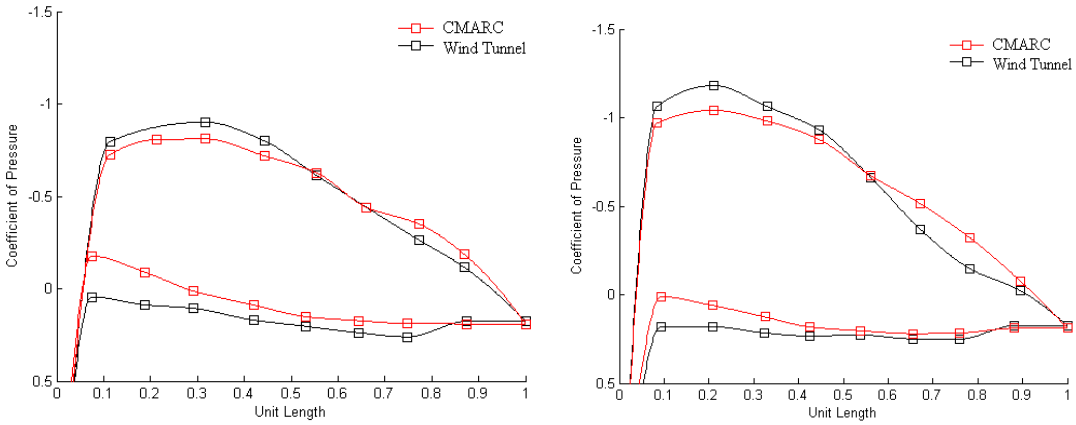

Alpha = 8 Degrees

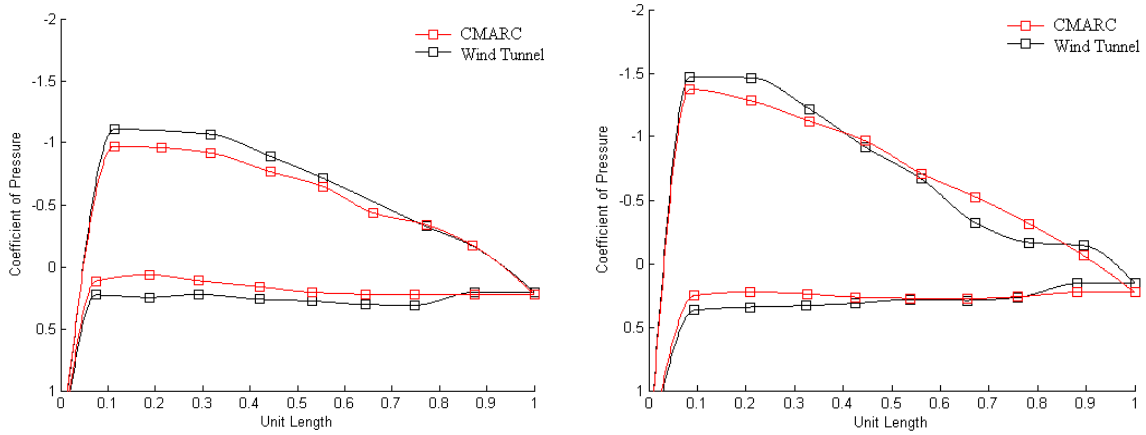

Alpha = 12 Degrees

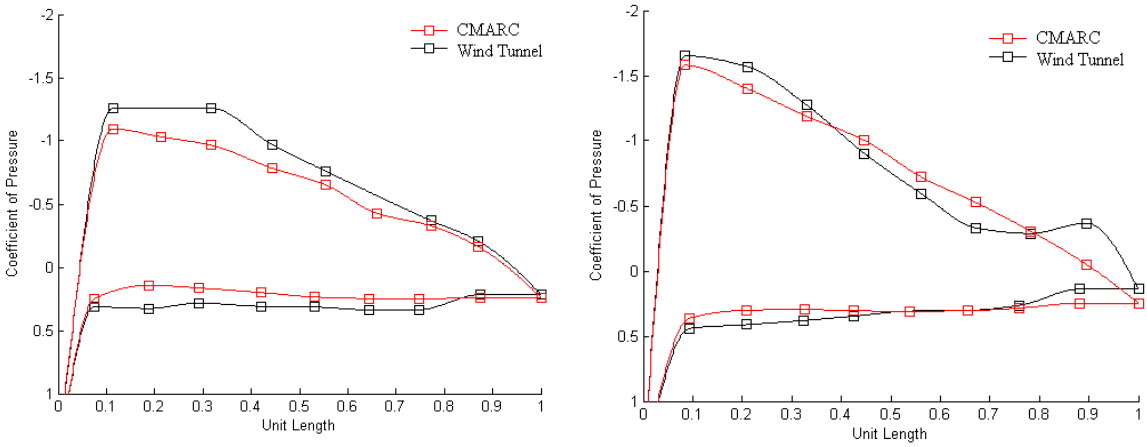

Alpha = 14 Degrees

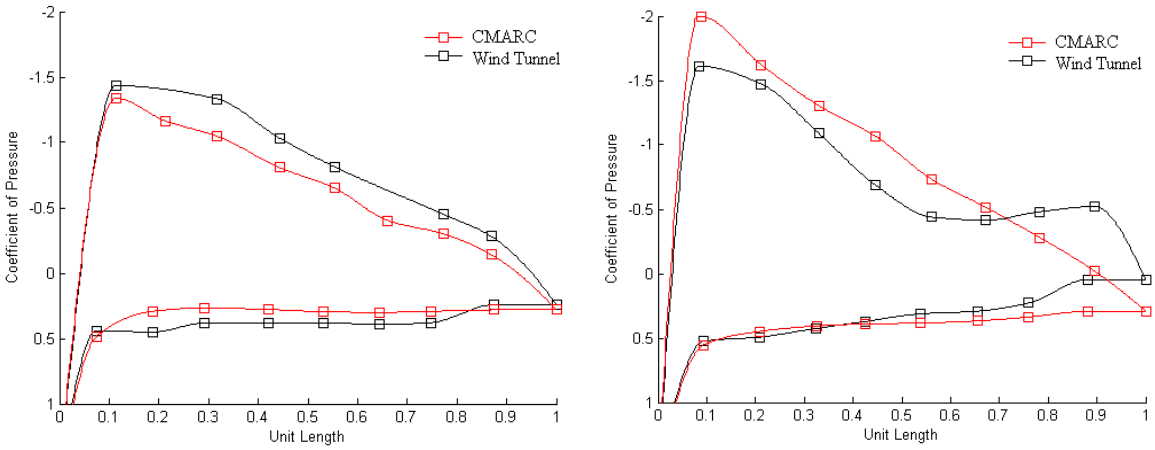

Alpha = 18 Degrees

8.4 Interpolation of Pressure Coefficients

```
%This program takes the known pressure coefficients and utilizes a cubic
%interpolation of the points to estimate the unknown pressures.  The local
%Cl value is then obtain by a simple integration.

%Change files for corresponding Alpha
xlower=dlmread(('q918.dat'),'\t',[0,0,9,0])
ylower=dlmread(('q918.dat'),'\t',[0,1,9,1])
xupper=dlmread(('q918.dat'),'\t',[10,0,19,0])
yupper=dlmread(('q918.dat'),'\t',[10,1,19,1])

%Look up 501 chordwise points
xlookup = 0:.002:1;

hold
figure(1)

%Generate pressures on the upper surface
ylookupupper = interp1(xupper,yupper,xlookup,'linear')
plot(xupper,yupper,'rs',xlookup,ylookupupper,'r-.') %,xlookup,f,'r')

%Generate pressures on the lower surface
ylookuplower = interp1(xlower,ylower,xlookup,'linear')
plot(xlower,ylower,'rs',xlookup,ylookuplower,'r-.') %,'g',xlookup,f,'r')

%Calculate the local lift coefficient summing the ylookup values and divide
%by the number of xlookup points
Cllin=(sum(ylookuplower)-sum(ylookupupper))/501


%Generate pressures on the upper surface
ylookupupper = interp1(xupper,yupper,xlookup,'spline')
plot(xupper,yupper,'rs',xlookup,ylookupupper,'g') %,xlookup,f,'r')

%Generate pressures on the lower surface
ylookuplower = interp1(xlower,ylower,xlookup,'spline')
plot(xlower,ylower,'rs',xlookup,ylookuplower,'g') %,'g',xlookup,f,'r')

Clspl=(sum(ylookuplower)-sum(ylookupupper))/501

%Generate pressures on the upper surface
ylookupupper = interp1(xupper,yupper,xlookup,'cubic')
plot(xupper,yupper,'rs',xlookup,ylookupupper,'b') %,xlookup,f,'r')

%Generate pressures on the lower surface
ylookuplower = interp1(xlower,ylower,xlookup,'cubic')
plot(xlower,ylower,'rs',xlookup,ylookuplower,'b') %,'g',xlookup,f,'r')
Clcub=(sum(ylookuplower)-sum(ylookupupper))/501

Cllin
Clcub
Clspl
```

8.5 Surface Tuft Figures

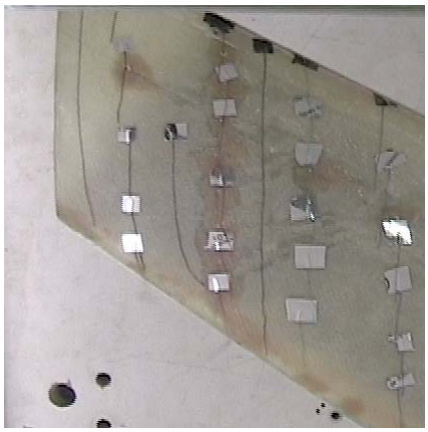


Alpha = -6 Degrees

Alpha = 6 Degrees


Alpha = 14 Degrees

8.6 Safety Factors for Final Design

	Component Description	Yield Stress (ksi.)	Maximum Stress (ksi.)	Safety Factor
Spar Structure	Main, <10 % Span	21.4	13.2	1.62
	Main, >10 % Span	17.8	11.1	1.60
	Main Mount Point	15.2	11.2	1.36
	Aft, <10 % Span	13.4	9.4	1.42
	Aft, >10 % Span	12.4	8.5	1.46
	Aft Mount Point	9.4	6.8	1.38
Skin Structure	<10 % Span, <13% Chord	8.0	5.3	1.51
	>10 % Span, <13% Chord	4.8	3.1	1.55
	<10 % Span, Between spars	10.3	7.4	1.35
	>10 % Span, Between spars	5.9	3.6	1.64
	<10 % Span, >58% Chord	3.3	2.4	1.38
	>10 % Span, >58% Chord	1.8	1.3	1.36

8.7 Strain Gage Coordinate Locations

Gage Number	X-Location	Y-Location	Z-Location
0*	22.00	0.00	-1.21
1	26.27	-2.08	-0.52
2	23.51	-6.25	-0.49
3	26.27	2.08	-0.52
4	21.53	-3.05	-1.18
5	21.53	-3.05	-1.18
6	21.53	3.05	-1.18
7	19.57	-6.53	-1.12
8	24.75	-4.00	-0.96
9	24.08	-2.50	-1.23

*Reference point at the leading edge of the root chord

8.8 Physical Load Test Plan

8.8.1 Procedure

1. Manufacture weights for point loads
2. Attach tailored wing to the load test stand
3. Connect wires with female locking connectors to the System 6000 scanner
4. Connect five strain gages with male locking connectors to the female connectors
5. Turn on the computer and the System 6000 scanner
6. Place weights on the table in front of the wing, i.e. loads at $\alpha = 0$ degrees, dynamic pressure = 10 psf.
7. After a minimum warm up time of 15 minutes, Zero and Calibrate the strain gages
8. Begin recording strain gage data
9. Place the weight on each side of the wing, beginning at the root and working outwards. If the strains exceed the maximum expected values in Appendix 8.8.2 for the selected strain gage, immediately reduce the remove the weights
10. Once the appropriate weights have been placed on the wing, record data for approximately 3 seconds
11. Remove the weights on each side of the wing, working from the wing tip inward
12. Stop and save the data once the strain values return to ~0 με
13. Repeat steps 6 through 12 for each load case and strain gage
14. Turn off the System 6000 scanner
15. Turn off the computer

8.8.2 Predicted Strain Values

Dynamic Pressure of 10 psf.		Microstrain								
Gage Number		**1**	**2**	**3**	**4**	**5**	**6**	**7**	**8**	**9**
Alpha (Degrees)	**0**	8	7	8	9	8.5	9	4	-33	30
	6	14	13	14	16	15	16	7	-58	52.5
	12	19	18.5	19	21	22	21	10	-85	75

Wing Loading Ratio of 50 to 1	Maximum Expected Microstrain								
Gage Number	**1**	**2**	**3**	**4**	**5**	**6**	**7**	**8**	**9**
	98	91	98	112	105	112	49	-406	368

8.8.3 Test Hazard Analysis

Test Hazard Analysis Worksheet	**Test Title:** Load Testing of the Tailored Wing
	Prepared By: David Roberts **Date:** 1-20-2006 **Phone:** 919-801-0703

Hazard Category **Subjective Probability of Occurrence**

	High	Probable	Uncertain	Remote	Improbable
Catastrophic					
Critical					
Marginal			**X**		
Negligible					

Hazards:

- Wing separation from the load test stand

Causes:

- Loose connection of the wing mount
- Structural failure of the wing due to the construction of the wing

Effects:

- Weights located on the wing will impact personnel
- Fragments from the wing could damage personnel

Minimizing Procedures:

- Wing mount was securely tightened and installed with lock nuts and washers
- Ensure that body parts are not under the table in which the test stand is mounted
- Wear safety glasses during each test

Emergency Procedures:

1. Immediately position yourself away from the test stand, Do Not attempt to grasp the weights
2. Remove any weights remaining on the table
3. If needed, contact Dr. Charles Hall and/or Mr. Stearns Heinzen
4. If needed, contact NCSU public safety

8.9 Strain Values

```
Program Strains
Character(10)::text
Character(25)::inputfile
Integer::i,j,count,elemnum,nodenum
Real,dimension(10000)::node,x,y,z
Real,dimension(10000,2000)::x_strain1,  y_strain1,  z_strain1, x_strain2,  y_strain2,  z_strain2
Real::d1,d2,d3,k1,k2,k3,k4
Real::strainavg(25)
Real::strain12, strain34
Real::errorx,errory,errorz
Real,dimension(25,25)::strain_gauge                    !straingage(#, x=1 y=2 z=3)
20 FORMAT(I9,6(F12.0))

! Reads the node coordinates in from ANSYS
OPEN(90,file="NLIST.txt",status='unknown')
count=0
Read(90,*)text
Read(90,*)text
Do i=1,5442
        Read(90,*)text
        If(text == "NODE")then
        Else
                count=count+1
    BACKSPACE(90)
                Read(90,*)node(count),x(count),y(count),z(count)
        End If
End Do

! Reads the node coordinates in from ANSYS
Write(*,*)"Input file for strains from ANSYS"
Read(*,*)inputfile
OPEN(99,file=inputfile,status='unknown')
elementnum=0
Do i=1,6980
        Read(99,*)text
        If(text == "NODE")then
        elemnum=elemnum+1
                !front / top strains
                Do j=1,4
        Read(99,20)nodenum,x_strain1(nodenum,elemnum),y_strain1(nodenum,elemnum),z_strain1(nodenum
,elemnum)
                End Do
                !back/aft or bottom/outside strains
                Do j=1,4
        Read(99,20)nodenum,x_strain2(nodenum,elemnum),y_strain2(nodenum,elemnum),z_strain2(nodenum
,elemnum)

                End Do
        End If
End Do
```

```
Write(*,*)"Enter error x,y,z (inches)"
Read(*,*)errorx,errory,errorz

!Strain gauge# and location
strain_gauge(1,1)=26.27+errorx
strain_gauge(1,2)=-2.08+errory
strain_gauge(1,3)=-0.52+errorz

strain_gauge(2,1)=23.51+errorx
strain_gauge(2,2)=-6.25+errory
strain_gauge(2,3)=-0.49+errorz

strain_gauge(3,1)=26.27+errorx
strain_gauge(3,2)=2.08+errory
strain_gauge(3,3)=-0.52+errorz

strain_gauge(4,1)=21.53+errorx
strain_gauge(4,2)=-3.05+errory
strain_gauge(4,3)=-1.18+errorz

strain_gauge(5,1)=21.53+errorx
strain_gauge(5,2)=-3.05+errory
strain_gauge(5,3)=-1.18+errorz

strain_gauge(6,1)=21.53+errorx
strain_gauge(6,2)=3.05+errory
strain_gauge(6,3)=-1.18+errorz

strain_gauge(7,1)=19.57+errorx
strain_gauge(7,2)=-6.53+errory
strain_gauge(7,3)=-1.12+errorz

strain_gauge(8,1)=24.75+errorx
strain_gauge(8,2)=-4.0+errory
strain_gauge(8,3)=-0.96+errorz

strain_gauge(9,1)=24.08+errorx
strain_gauge(9,2)=-2.5+errory
strain_gauge(9,3)=-1.23+errorz
!Interpolation
!Strain gauge1,3
          d1 = sqrt(  0.0**2.0  +  0.0**2.0  +  (z(439)-z(5047))**2.0  )
          k1 = sqrt(  (0.0)**2.0  +  0.0**2.0  +  (strain_gauge(1,3)-z(5047))**2.0  )
          k2=abs(d1-k1)
          strain12 = (y_strain2(5047,1683)*k1+y_strain2(439,1683)*k2)/d1

          d1 = sqrt(  0.0**2.0  +  0.0**2.0  +  (z(463)-z(5051))**2.0  )
          k1 = sqrt(  (0.0)**2.0  +  0.0**2.0  +  (strain_gauge(1,3)-z(5051))**2.0  )
          k2=abs(d1-k1)
          strain34 = (y_strain2(5051,1683)*k1+y_strain2(463,1683)*k2)/d1
          d3 = sqrt(   0.0**2.0  +  (y(439)-y(463))**2.0  +  0.0**2.0 )
          k3 = sqrt(   0.0**2.0  +  (strain_gauge(1,2)-y(463))**2.0  +  0.0**2.0 )
          k4=abs(d3-k3)
          Strainavg(1) = (strain12*k3+strain34*k4)/d3
          Strainavg(3)=Strainavg(1)
```

```
!Strain gauge2
        d1 = sqrt(  0.0**2.0  +  0.0**2.0  +  (z(679)-z(5087))**2.0  )
        k1 = sqrt(  0.0**2.0  +  (0.0)**2.0  +  (strain_gauge(2,3)-z(5087))**2.0  )
        k2=abs(d1-k1)
        strain12 = (y_strain2(5087,1703)*k1+y_strain2(679,1703)*k2)/d1

        d1 = sqrt(  0.0**2.0  +  0.0**2.0  +  (z(703)-z(5091))**2.0  )
        k1 = sqrt(  0.0**2.0  +  (0.0)**2.0  +  (strain_gauge(2,3)-z(5091))**2.0  )
        k2=abs(d1-k1)
        strain34 = (y_strain2(5091,1703)*k1+y_strain2(703,1703)*k2)/d1

        d3 = sqrt(   0.0**2.0  +  (y(679)-y(703))**2.0  +  0.0**2.0 )
        k3 = sqrt(   0.0**2.0  +  (strain_gauge(2,2)-y(703))**2.0  +  0.0**2.0 )
        k4=abs(d3-k3)
        Strainavg(2) = (strain12*k3+strain34*k4)/d3

!Strain gauge4,6
        d1 = sqrt(  0.0**2.0  +  0.0**2.0  +  (z(4900)-z(3875))**2.0  )
        k1 = sqrt(  0.0**2.0  +  0.0**2.0  +  (strain_gauge(4,3)-z(3875))**2.0  )
        k2=abs(d1-k1)
        strain12 = (y_strain1(3875,1612)*k1+y_strain1(4900,1612)*k2)/d1

        d1 = sqrt(  0.0**2.0  +  0.0**2.0  +  (z(4904)-z(3863))**2.0  )
        k1 = sqrt(  0.0**2.0  +  0.0**2.0  +  (strain_gauge(4,3)-z(3863))**2.0  )
        k2=abs(d1-k1)
        strain34 = (y_strain1(3863,1612)*k1+y_strain1(4904,1612)*k2)/d1

        d3 = sqrt(   0.0**2.0  +  (y(4900)-y(4904))**2.0  +  0.0**2.0 )
        k3 = sqrt(   0.0**2.0  +  (strain_gauge(4,2)-y(4904))**2.0  +  0.0**2.0 )
        k4=abs(d3-k3)
        Strainavg(4) = (strain12*k3+strain34*k4)/d3
        Strainavg(6)=Strainavg(4)

!Strain gauge5
        d1 = sqrt(  0.0**2.0  +  0.0**2.0  +  (z(4900)-z(3875))**2.0  )
        k1 = sqrt(  0.0**2.0  +  0.0**2.0  +  (strain_gauge(5,3)-z(3875))**2.0  )
        k2=abs(d1-k1)
        strain12 = (y_strain2(3875,1612)*k1+y_strain2(4900,1612)*k2)/d1

        d1 = sqrt(  0.0**2.0  +  0.0**2.0  +  (z(4904)-z(3863))**2.0  )
        k1 = sqrt(  0.0**2.0  +  0.0**2.0  +  (strain_gauge(5,3)-z(3863))**2.0  )
        k2=abs(d1-k1)
        strain34 = (y_strain2(3863,1612)*k1+y_strain2(4904,1612)*k2)/d1

        d3 = sqrt(   0.0**2.0  +  (y(4900)-y(4904))**2.0  +  0.0**2.0 )
        k3 = sqrt(   0.0**2.0  +  (strain_gauge(5,2)-y(4904))**2.0  +  0.0**2.0 )
        k4=abs(d3-k3)
        Strainavg(5) = (strain12*k3+strain34*k4)/d3
```

```
!Strain gauge7
        d1 = sqrt(  0.0**2.0  +  0.0**2.0  +  (z(4936)-z(3767))**2.0  )
        k1 = sqrt(  0.0**2.0  +  0.0**2.0  +  (strain_gauge(7,3)-z(3767))**2.0  )
        k2=abs(d1-k1)
        strain12 = (y_strain1(3767,1630)*k1+y_strain1(4936,1630)*k2)/d1

        d1 = sqrt(  0.0**2.0  +  0.0**2.0  +  (z(4940)-z(3755))**2.0  )
        k1 = sqrt(  0.0**2.0  +  0.0**2.0  +  (strain_gauge(7,3)-z(3755))**2.0  )
        k2=abs(d1-k1)
        strain34 = (y_strain1(3755,1630)*k1+y_strain1(4940,1630)*k2)/d1

        d3 = sqrt(   0.0**2.0  +  (y(4936)-y(4940))**2.0  +  0.0**2.0 )
        k3 = sqrt(   0.0**2.0  +  (strain_gauge(7,2)-y(4940))**2.0  +  0.0**2.0 )
        k4=abs(d3-k3)
        Strainavg(7) = (strain12*k3+strain34*k4)/d3

!Strain gauge8
        d1 = sqrt(  (x(559)-x(4736))**2.0  +  0.0**2.0  +  0.0**2.0  )
        k1 = sqrt(  (strain_gauge(8,1)-x(4736))**2.0 + 0.0**2.0  +  0.0**2.0  )
        k2=abs(d1-k1)
        strain12 = (x_strain1(4736,1542)*k1+x_strain1(559,1542)*k2)/d1

        d1 = sqrt(  (x(583)-x(4711))**2.0  +  0.0**2.0  +  0.0**2.0  )
        k1 = sqrt(  (strain_gauge(8,1)-x(583))**2.0 +(0.0)**2.0  +  (0.0)**2.0  )
        k2=abs(d1-k1)
        strain34 = (x_strain1(583,1542)*k1+x_strain1(4711,1542)*k2)/d1

        d3 = sqrt(   0.0**2.0  +  (y(559)-y(583))**2.0  +  0.0**2.0 )
        k3 = sqrt(   0.0**2.0  +  (strain_gauge(8,2)-y(583))**2.0  +  0.0**2.0 )
        k4=abs(d3-k3)
        Strainavg(8) = (strain12*k3+strain34*k4)/d3

!Strain gauge9
        d1 = sqrt(  (x(4827)-x(4828))**2.0  +  0.0**2.0  +  0.0**2.0  )
        k1 = sqrt(  (strain_gauge(9,1)-x(4828))**2.0  +  0.0**2.0  +  0.0**2.0  )
        k2=abs(d1-k1)
        strain12 = (y_strain2(4828,1574)*k1+y_strain2(4827,1574)*k2)/d1

        d1 = sqrt(  (x(4802)-x(4799))**2.0  +  0.0**2.0  +  0.0**2.0  )
        k1 = sqrt(  (strain_gauge(9,1)-x(4799))**2.0  +  0.0**2.0  +  0.0**2.0  )
        k2=abs(d1-k1)
        strain34 = (y_strain2(4799,1574)*k1+y_strain2(4802,1574)*k2)/d1

        d3 = sqrt(   0.0**2.0  +  (y(4827)-y(4802))**2.0  +  0.0**2.0 )
        k3 = sqrt(   0.0**2.0  +  (strain_gauge(9,2)-y(4802))**2.0  +  0.0**2.0 )
        k4=abs(d3-k3)
        Strainavg(9) = (strain12*k3+strain34*k4)/d3

Do i=1,9
        write(*,*)"Strain at Gauge",i," = ",strainavg(i)
End Do
pause
End Program
```

8.10 Physical Load Test Plots

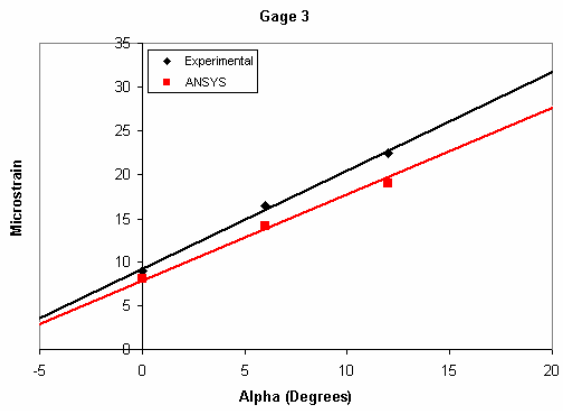

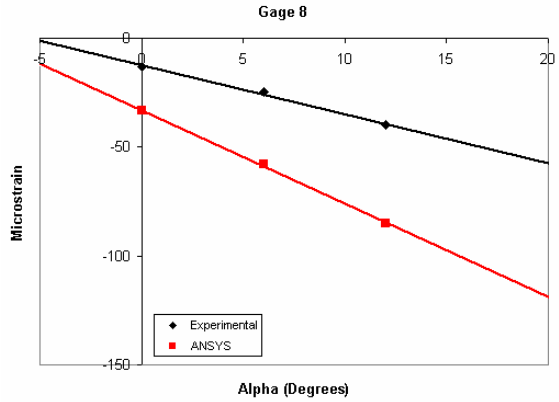

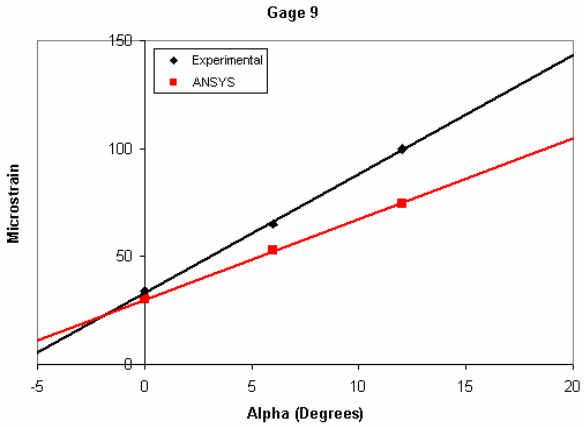

8.11 Wind Tunnel Test Plan

8.11.1 Procedure

1. Attach tailored wing to the wind tunnel mount
2. Secure strain gage wires to the sting
3. Set wing at 0 degrees angle of attack using the digital level
4. Connect wires with female locking connectors to the System 6000 scanner
5. Connect five strain gages with male locking connectors to the female connectors
6. Turn on the computer and the System 6000 scanner
7. Turn on the wind tunnel, Do NOT start the wind tunnel
8. After a minimum warm up time of 15 minutes, Zero and Calibrate the strain gages
9. Begin recording strain gage data
10. Start the wind tunnel
11. Increase the dynamic pressure to 10 psf. If the strains exceed the maximum expected values in Appendix 8.8.2 for the selected strain gage, immediately reduce the dynamic pressure
12. Record data for approximately 3 seconds
13. While monitoring the strain values, increase the angle of attack by increments of 2 degrees.
14. Once an angle of attack of 18 degrees has been achieved, reduce the dynamic pressure to 0.5 psf. and stop the wind tunnel
15. Stop and save the data once the strain values return to ~0 με
16. Once data for all strain gages has been taken, turn off the wind tunnel
17. Turn off the System 6000 scanner
18. Turn off the computer

8.11.2 Test Hazard Analysis

Test Hazard Analysis Worksheet

Test Title: Wind Tunnel Testing of the Tailored Wing

Prepared By: David Roberts **Date:** 1-30-06
Phone: 919-801-0703

Hazard Category **Subjective Probability of Occurrence**

	High	Probable	Uncertain	Remote	Improbable
Catastrophic					
Critical				**X**	
Marginal					
Negligible					

Hazards:

- Wing separation from the wind tunnel mount

Causes:

- Loose connection of the wing mount
- Structural failure of the wing due to the construction of the wing

Effects:

- The wing will exceed blockage limits of the wind tunnel upon impact with the screens
- Fragments from the wing could collide and damage the fan blades

Minimizing Procedures:

- Wing mount was securely tightened and installed with lock nuts and washers
- Wing was designed to withstand any aerodynamic loads produced in the NCSU wind tunnel
- Ensure screen is thoroughly secured

Emergency Procedures:

1. Immediately stop tunnel with the control console stop button and return fan blades their original location
2. Shut down power to the wind tunnel
3. Contact Dr. Charles Hall and/or Mr. Stearns Heinzen
4. If needed, contact NCSU public safety

8.12 Wind Tunnel Plots